



The nature of strong Brønsted acidity of Ni-SMM clay



Chaochao Yue^a, Chong Liu^a, Brahim Mezari^a, Angelika Brückner^b, Evgeny A. Pidko^a,
Marcello S. Rigutto^c, Emiel J.M. Hensen^{a,*}

^a Inorganic Materials Chemistry, Eindhoven University of Technology, P.O. Box 513, 5600 MB Eindhoven, The Netherlands

^b Leibnitz Institut für Katalyse, Albert Einsteinstrasse 29a, 18059, Rostock, Germany, Germany

^c Shell Global Solutions International B.V., P.O. Box 38000, 1030 BN Amsterdam, The Netherlands

ARTICLE INFO

Article history:

Received 5 December 2015

Received in revised form 28 February 2016

Accepted 4 March 2016

Available online 8 March 2016

Keywords:

Acidity

Clay

Ni-SMM

IR spectroscopy

DFT calculations

ABSTRACT

The origin of the high Brønsted acidity of Ni-SMM (Ni-substituted synthetic mica-montmorillonite; beidellite structure) clays was investigated. Ni-SMM clays with varying F content, SMM with F and Ni-SMM without F in the structure were synthesized under hydrothermal conditions. Ni-SMM clays with intermediate F content contained very strong Brønsted acid sites. The optimum Ni-SMM sample outperformed zeolites such as H-ZSM-5 and H-USY (ultrastabilized Y) in alkane hydroisomerization. Infrared spectroscopy with different probe molecules shows that Ni-SMM contains two types of BAS. In addition to acid sites also observed in other clays and amorphous silica-alumina, Ni-SMM contains a small number of acid sites that are stronger than the acid sites in zeolites. The number of such sites does not depend on Ni-SMM reduction. A small amount of strongest Brønsted acid sites positions the catalytic activity of Ni-SMM clay beyond that of zeolites. Periodic density functional theory calculations show that the substitution of octahedral $[\text{Al}^{3+}\text{-O}]^+$ by $[\text{Ni}^{2+}\text{-F}]^+$ causes high acidity of the interlayer proton connected to the aluminium-occupied tetrahedron. This explains why Ni-SMM (no F in the structure) and SMM with F (no Ni in the structure; F replaces only structural OH) exhibit conventional clay acidity. The presence of Ni in the octahedral layer leads to isomorphous substitution of bridging O anions that connect the octahedral with the tetrahedral layer by F. The electron-withdrawing nature of the bridging F induces the unusually high acidity of the interlayer protons in Ni-SMM.

© 2016 Elsevier B.V. All rights reserved.

1. Introduction

Solid acids constitute an important class of heterogeneous catalysts, widely used in the chemical industry. Porous aluminosilicates such as zeolites, clays and amorphous mixed silica-alumina phases find widespread application in such processes as fluid catalytic cracking, hydrocracking and hydroisomerization of petroleum feedstock. The acidity of aluminosilicates is due to charge compensation by protons of the negative charge that results from Si^{4+} substitutions by Al^{3+} in the silica network [1]. For aluminosilicates, Brønsted acidity decreases in the order zeolite > clay > amorphous silica-alumina. It is usually assumed that the crystalline zeolite framework embeds stronger Brønsted acid sites (BAS) than clays and amorphous silica-alumina materials. Zeolites and amorphous silica-alumina are made up from silica networks in which the dilution of the tetrahedral Al centers plays an important role in

the acidity [2]. Clays, on the other hand, are layered aluminosilicate materials in which usually tetrahedral (T) silicate sheets are separated from each other by layers containing octahedrally (O) coordinated cations [3]. These T-O-T layers are negatively charged because of Al^{3+} for Si^{4+} substitutions in the silicate sheets. Another way of inducing charges in the T-O-T layers is by variation of the composition of the octahedral sheet. Accordingly, the acidity situation in clays is more complex than in zeolites. Substitutions in the octahedral layers of clays seem to cause their strong acidity [4].

Acid-treated montmorillonite clays were the early catalysts used for the cracking of petroleum feedstock to more valuable products. These clays were replaced by synthetic silica-alumina cracking catalysts in the 1950s and then by zeolites in the 1960s. HF-treated montmorillonite was also used as the acid component of catalysts in early hydrocracking processes. Synthetic mica-montmorillonite (SMM) has attracted significant attention in the past as an acidic catalyst for such important reactions as oligomerization of olefins as well as hydrocracking and hydroisomerization of hydrocarbons [5–10]. Its hydrothermal synthesis was disclosed in a patent by Capell and Granquist [5]. The SMM name derives from the understanding that this clay has the 2:1 layer aluminosilicate structure

* Corresponding author.

E-mail addresses: marcello.rigutto@shell.com (M.S. Rigutto),
e.j.m.hensen@tue.nl (E.J.M. Hensen).

composed of interstratified expandable montmorillonite-like and non-expandable mica-like layers [6]. It was later realized that SMM has the beidellite structure [11]. Beidellite is also a 2:1 phyllosilicate, similar to montmorillonite, consisting of two tetrahedral sheets sandwiching the central octahedral sheet. In beidellite, the cationic exchange capacity mainly derives from Al^{3+} for Si^{4+} substitutions in the tetrahedral sheet. There are six octahedral positions in each unit cell with a net charge of -12 . When this is achieved by four Al^{3+} ions, dioctahedral clay is obtained. The octahedral Al^{3+} ions can be replaced by divalent ions resulting in trioctahedral or, when not all Al^{3+} are replaced, in mixed dioctahedral-trioctahedral synthetic clays [12]. SMM consists of platelets that are made up of the stacked parallel 2:1 layers. Exchange ions, which balance the charge of the octahedral and tetrahedral layers, occupy sites in the interlayer space and at the platelet edges. The isomorphous substitution of octahedral Al^{3+} by Co^{2+} or Ni^{2+} in SMM results in strongly acidic clays that surpass the acidity of SMM and other clays such as saponites [13,14].

Pyridine has been frequently used to characterize the acid sites in SMM clay. The number of acid sites of SMM is lower than in zeolites [15]. Accordingly, one would expect the catalytic activity of SMM to be low compared with zeolites. However, this is not the case. In particular, metal-substituted SMM such as Ni-SMM and Co-SMM display high Brønsted acidity. The reason for the high acidity of Ni-SMM is not well understood. Pyridine IR measurements demonstrated that the acid site density increases when part of the Ni cations are reduced. The acid site density in reduced Ni-SMM remained constant after metallic Ni was removed as $\text{Ni}(\text{CO})_4$ [16]. Geus and co-workers mentioned that reduction of divalent cations at interlayer positions, which in this way neutralize the negative layer charge, increases the number of acid sites [17]. In line with this, Heinerman et al. found that reduced Ni-SMM contains more ammonium ions than unreduced Ni-SMM [16]. It is generally assumed that the Brønsted acidity of clay minerals such as beidellite, montmorillonite and saponite is relatively weak compared with zeolites. Recently, it has been demonstrated that the strength of the BAS in Mg-saponite is only slightly lower than that of the acid sites in zeolites [18]. The lower overall acidity of Mg-saponite is due to the smaller amount of acid sites in the clay [19]. The positive effect of isomorphous substitution of Ni or Co into SMM clay may be related to the intrinsic strength of the acid sites. The high acidity of Ni-SMM has for instance been linked to the interaction of highly dispersed Ni clusters with silica [20–23]. In addition to interlayer acidity (acidity due to OH groups located at the silicate sheets), it has also been suggested that the strong acid sites can be located at the edges of the clay platelets [24]. Van Santen reasoned that the reduction of octahedral Ni^{2+} plays a role in generating strong acidic OH groups at such locations [24].

Similar to zeolites, clay minerals can be synthesized under hydrothermal conditions [25]. Usually, higher temperatures are required to obtain well-crystallized clays. The use of fluoride in the synthesis of SMM improves its thermal stability [3]. The replacement of structural OH groups by fluorine is well known and has been argued to increase the crystallinity and acidity of zeolites and other aluminosilicate materials [26–29]. The replacement of surface O or OH groups by F has also been mentioned as a cause of higher acidity [30].

In this work, we set out to better understand the nature of the acid sites in Ni-SMM. A range of Ni-SMM clays was prepared by varying the amount of NH_4F in the synthesis gel. This parameter has not been investigated in a systematic manner yet. Next to acidity characterization by CO and pyridine IR, we follow the isotopic exchange of OH groups with deuterated benzene by IR spectroscopy [17]. Applied to Ni-SMM, we can distinguish a relatively small population of strong BAS from a large amount of structural OH groups; the acid strength of these sites surpasses that of zeolite protons.

Consistent with this, Ni-SMM catalysts outperform zeolites in the bifunctional hydroisomerization of *n*-heptane. The roles of Ni and F and the reduction of structural Ni^{2+} ions were investigated in more detail. Amongst others, periodic density functional theory calculations were used to understand the influence of different substitution schemes for SMM clay on the acidity of various bridging OH groups present at the silicate sheets.

2. Experimental

2.1. Synthesis of materials

2.1.1. Ni-SMM

Ni-SMM catalyst was synthesized according to the procedure given by Heinerman et al. [16]. 8.4 g sodium silicate solution dispersed in 90 g water was exchanged three times with Amberlite IR 120-H cation resin. Then, 6 g nickel acetate ($\text{Ni}(\text{C}_2\text{H}_3\text{O}_2)_2 \cdot 4\text{H}_2\text{O}$) dissolved in 30 g H_2O was mixed while stirring to disperse the silica. 5.64 g aluminum isopropoxide and 0.18 g ammonia fluoride were added to the mixture. The resulting slurry was heated under continuous stirring to remove water until the volume was about 70 ml. An amount of 1.2 ml of aqueous ammonia (25% NH_3 in water) was added and the final slurry was transferred to a glass container and placed in a stainless-steel autoclave. The temperature was increased to 300 °C in about 3 h and kept at this temperature for 40 h. The product was obtained through filtration and then washed with water and dried in a stove at 110 °C overnight. The sample was then calcined in air at 540 °C for 6 h after heating to this temperature at 3 °C/min. This sample was denoted as Ni-SMM-0.18F, the suffix denoting the amount of NH_4F in g during synthesis. Other Ni-SMM clays were prepared with 0, 0.9, 1.8 and 3.6 g NH_4F in the synthesis gel.

2.1.2. Beidellite (SMM)

Beidellite was synthesized according to a literature procedure [15]. 3.52 g $\text{SiO}_2/\text{Al}_2\text{O}_3$ (25% Al_2O_3), 2.688 g aluminum isopropoxide and 0.364 g NH_4F were mixed in water. The resulting mixture was stirred and placed in a glass-lined stainless-steel autoclave. The product was retrieved by filtration after hydrothermal treatment at 300 °C for 16 h and subsequent drying and calcination in the manner described for Ni-SMM.

Pd/Ni-SMM hydroisomerization catalysts were prepared from these clays by impregnating 1.5 g Ni-SMM or SMM with 15 g of a solution of tetraaminepalladium nitrate (Sigma-Aldrich, 10wt% in water) to reach a final Pd loading of 1.0wt%. The excess solvent was evaporated and the materials were further dried at room temperature followed by calcination in air at 300 °C for 2 h. The obtained catalysts are denoted as Pd/Ni-SMM.

2.2. Characterization

Powder X-ray diffraction (XRD) patterns were measured on a Bruker Phaser D2 Endeavor powder diffraction system using $\text{Cu K}\alpha$ radiation (1.5406 Å) with a scanning speed of 0.0162/step. Nitrogen sorption isotherms were measured on a Micromeritics Tristar 3000 system in static measurement mode. The samples were outgassed at 120 °C for 3 h prior to the sorption measurements. The specific area was determined by the Brunauer-Emmett-Teller (BET) method applied to adsorption data in the range $p/p_0 = 0.05$ –0.25. Temperature programmed reduction (TPR) experiments were carried out in a flow apparatus equipped with a fixed-bed reactor, a computer-controlled oven and a thermal conductivity detector. Prior to TPR, the catalyst was treated by a flowing mixture of 4vol% O_2 in He at 30 °C. Then, the sample was reduced in 4 vol% H_2 in N_2 at a flow rate of 8 ml/min, while heating from room temperature to 800 °C at a rate of 10 °C/min and keeping the sample isothermal at 800 °C

for 60 min. The H₂ signal was calibrated using a CuO/SiO₂ reference. Scanning electron microscopy (SEM) was performed using a Philips environmental scanning electron microscope FEIXL-30 ESEM FEG in high-vacuum mode at low voltage.

Nuclear Magnetic Resonance (NMR) spectra were recorded on a 11.7 T Bruker DMX500 NMR spectrometer operating at 500 MHz for ¹H, 132 MHz for ²⁷Al and 470 MHz for ¹⁹F. The MAS NMR spectra were performed using a Bruker 2.5-mm MAS probehead spinning at 30 kHz. ²⁷Al NMR spectra were recorded with a single pulse sequence with an 18° pulse duration of 1 μs and a interscan delay of 1 s. ¹H and ¹⁹F NMR spectra were carried out using a rotor synchronized Hahn-echo pulse sequence p1-τ1-p2-τ2-aq with a 90° pulse p1 = 5 μs and a 180° pulse p2 = 10 μs. Interscan delays of 10 s and 1 s were chosen for ¹H and ¹⁹F, respectively. The ¹H NMR shift was calibrated using tetramethylsilane (TMS); a saturated Al(NO₃)₃ solution was used for ²⁷Al NMR shift calibration. The ¹⁹F NMR chemical shift was referenced to CCl₃ using C₆F₆ (−164.9 ppm) as external standard. Prior to ²⁷Al MAS NMR measurements the samples were fully saturated with water. For ¹H MAS NMR measurements, the sample was dehydrated at 150 °C at a pressure lower than 10^{−5} mbar for a duration of 3 h.

Electron paramagnetic resonance (EPR) spectroscopy was carried out at the Leibnitz Institute for Catalysis. An amount of 15 mg of each catalyst was placed in a home-made EPR in situ cell consisting of a 3 mm quartz tube with an implemented quartz capillary connected to gas lines. Spectra were recorded at room temperature and at 100 K of the calcined clay and after 16 h treatment in 5% H₂ in N₂ flow at 450 °C and at 550 °C. EPR spectra in X-band (ν ≈ 9.5 GHz) were recorded on a Bruker ELEXSYS 500-10/12 cw spectrometer using a microwave power of 6.3 mW for calcined samples and of 0.6 mW for reduced samples, a modulation frequency of 100 kHz and a modulation amplitude of 0.5 mT.

The isotopic H/D exchange between hydroxyl groups and adsorbed perdeuterobenzene was followed by IR spectroscopy. IR spectra were recorded on a Bruker Vertex V70v FTIR spectrometer in transmission mode. The powdered sample was pressed into a self-supporting wafer with a density ρ = 9–11 mg/cm² and placed inside a controlled environment infrared transmission cell, capable of heating and cooling, gas dosing and evacuation. After calcination at 550 °C, the catalyst wafer was evacuated to a pressure lower than 2 × 10^{−6} mbar and temperature was lowered to 30 °C. A background spectrum was recorded. Perdeuterobenzene (C₆D₆, Merck, purity 99.96%) was introduced into the cell from a glass ampoule. The total volume of C₆D₆ administered to the cell was 0.33 mmol ± 1% (pressure of 10 mbar). The sample was exposed to perdeuterobenzene for 10 s followed by evacuation for 30 min. Then, a next spectrum of the partially exchanged sample was recorded. This sequence was automatically repeated with exposure times of 30 s, 5 min, 10 min, 20 min, 30 min at 30 °C, 30 min at 50 °C, 30 min at 150 °C and 30 min at 250 °C. For each spectrum, 128 scans were accumulated at a resolution of 2 cm^{−1}. Difference spectra were obtained by subtracting the initial spectrum of the dehydrated sample from the spectra after exposure to C₆D₆.

For IR spectroscopy of adsorbed CO (CO_{ads} IR), a similar setup was used as for the H/D exchange measurements. After calcination and outgassing at 550 °C, the sample was cooled to 90 K. A background spectrum was recorded at this temperature. CO was then introduced into the cell in small doses via a sample loop and spectra were recorded at increasing CO coverage. IR spectroscopy of adsorbed pyridine (Py_{ads} IR) was done in a similar manner. After calcination, a background spectrum was recorded at 150 °C. The sample was then exposed to pyridine at 150 °C for 30 min. After evacuation at 150 °C for 1 h to remove physisorbed pyridine, a spectrum was recorded. Additional spectra were recorded at 150 °C after outgassing at 200 °C, 300 °C and 400 °C for 1 h.

2.3. Catalytic activity measurements

The catalytic performance of Pd-loaded clays and reference materials in the hydroisomerization of *n*-heptane was determined in a microflow reactor setup. Prior to testing, the sample was calcined at 300 °C and reduced at 440 °C at 35 bar in flowing hydrogen. Hydroisomerization of *n*-heptane was carried out at 35 bar at a molar H₂/hydrocarbon ratio of 24. The initial reaction temperature was 440 °C. The reaction temperature was lowered to 200 °C at a rate of 0.2 °C/min. The catalytic activity is expressed as the temperature for which the *n*-heptane conversion was 40%. From this temperature, relative values for the rate constant *k* for two catalysts at a reference temperature *T*_{ref} can be determined using the expression

$$\ln(k_1/k_2) = E_{\text{act},1}/R_g(1/T_{40,1} - 1/T_{\text{ref}}) - E_{\text{act},2}/R_g(1/T_{40,2} - 1/T_{\text{ref}}) \quad (1)$$

or, if we choose the second catalyst as the reference *T*_{ref} = *T*_{40,2}

$$\ln(k/k_{\text{ref}}) = E_{\text{act}}/R_g(1/T_{40} - 1/T_{40,\text{ref}}) \quad (2)$$

in which *E*_{act} is the activation energy (J/mol) and *R*_g the gas constant (J/mol.K). In this work, we have chosen H-ZSM-5 zeolite with a Si/Al ratio of 20 (Akzo-Nobel Catalysts, now Albemarle) as the reference aluminosilicate.

2.4. Density functional theory calculations

Density functional theory (DFT) calculations were performed using the Vienna Ab initio Simulation Package (VASP) [31–34]. The PBE exchange-correlation functional was used in all calculations [35]. The electron-ion interactions were described with the projected-augmented waves (PAW) method [36,37]. The valence electrons were treated using a plane-wave basis set with a kinetic energy cut-off of 500 eV. A Monkhorst-Pack grid of 2 × 2 × 1 was used to sample the Brillouin zone [38]. The DFT-D3(BJ) dispersion correction method of Grimme was employed to account for the van der Waals interactions [39]. A modest Gaussian smearing was applied to band occupations around the Fermi level, and the total energies were extrapolated to σ → 0. Periodic boundary conditions were employed in all calculations. The parameters of the unit cell (*a* = 5.17 Å, *b* = 8.98 Å, *c* = 15.00 Å and α = β = γ = 90°) reported by Viani et al. were used to construct the beidellite structure [40]. The composition of our reference SMM model is H⁺[Al₄O₈(OH)₄][Si₇AlO₁₂], that is Al ions occupy 4 out of 6 cationic positions in the octahedral layer and the tetrahedral layer contains one Al ion, giving rise to a charge-compensating proton located at a bridging O atom of the tetrahedral layer. Various substitutions were made in the reference SMM model and the acidity of the interlayer OH group was probed by computing the change in the OH stretch frequency before and after CO adsorption. Full geometry optimizations were performed with fixed cell parameters. The system was assumed to be converged when the forces on each atom were below 0.05 eV/Å.

As a reference, we also determined in a similar manner the acidity of faujasite models with varying framework Si/Al ratio. We used a rhombohedral unit cell [41] and substituted framework Si atoms by Al to obtain three models with Si/Al ratios of 2.4, 7, and 47 with, respectively, 14, 6, and 1 framework Al per unit cell. The computations were carried out at the same DFT accuracy as done for the SMM models, except that the Brillouin zone sampling was restricted to the *Γ* point. For the three zeolite models with different Si/Al ratio, the parameters of the unit cells were firstly optimized (Si/Al = 2.4: *a* = *b* = *c* = 17.65 Å, α = β = γ = 60°; Si/Al = 7: *a* = *b* = *c* = 17.44 Å, α = β = γ = 60°; Si/Al = 47:

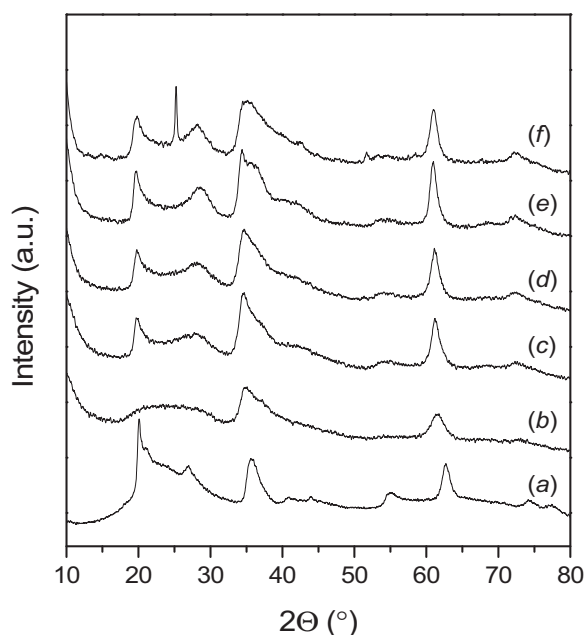


Fig. 1. XRD patterns of (a) SMM and (b–f) Ni-SMM prepared with different amounts of NH_4F in the gel: (b) Ni-SMM-0F, (c) Ni-SMM-0.18F, (d) Ni-SMM-0.9F, (e) Ni-SMM-1.8F and (f) Ni-SMM-3.6F.

Table 1
Physico-chemical properties of SMM and Ni-SMM clay materials.

Sample	Al (wt%)	Ni (wt%)	F (wt%)	S_{BET} (m^2/g)	d_{BET} (nm)
Ni-SMM-0F	12.4	21.5	<0.1	297	9.3
Ni-SMM-0.18F	13.6	24.2	0.7	183	9.4
Ni-SMM-0.9F	12.5	23.3	1.3	191	5.8
Ni-SMM-1.8F	9.1	25.4	1.9	146	4.4
Ni-SMM-3.6F	7.5	23.2	6.9	247	4.5
SMM	17.3	<0.1	0.33	140	21.9

$a = b = c = 17.29 \text{ \AA}$, $\alpha = \beta = \gamma = 60^\circ$). The geometry of the fixed models was then optimized in the presence of CO close to the proton.

3. Results and discussion

3.1. Physico-chemical characterization

Fig. 1 shows the XRD patterns of the SMM and Ni-SMM materials prepared by hydrothermal synthesis at 300°C . All Ni-SMM materials have the same structure as the beidellite structure of SMM [16]. The (060) reflection for the beidellite clay is at slightly higher 2θ (62.8°) than for the Ni-SMM clays ($60.9\text{--}61.5^\circ$). This relates to the dioctahedral nature of beidellite with only trivalent Al in the octahedral layer, whereas the Ni-SMM materials are mixed dioctahedral-trioctahedral clays containing also substantial amounts of divalent Ni in the octahedral layer. The crystallinity of the Ni-SMM samples increases with the amount of F in the starting gel. This trend is consistent with the findings of Huve et al. about the role of F on the crystallinity of pure beidellite [42]. The mineralizing role of F in zeolite synthesis is well known and relates to the higher solubility of inorganic metal fluorides as compared with the corresponding hydroxides [43]. The XRD pattern of Ni-SMM-3.6F contains an additional sharp reflection at $2\theta = 25.2^\circ$, which is due to AlF_3 [44].

Table 1 lists the basic characterization results for these materials. All Ni-SMM materials have comparable Ni content. The incorporation of Ni in the SMM structure mainly occurs through isomorphous substitution of octahedral Al^{3+} ions by Ni^{2+} ions,

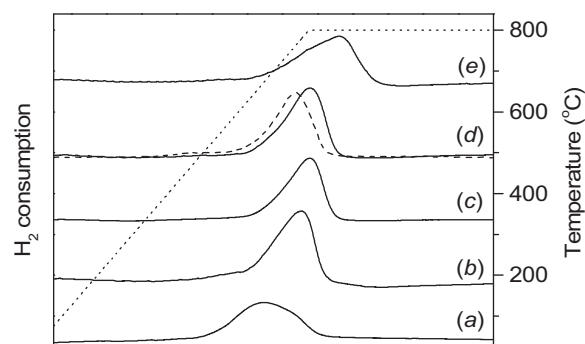


Fig. 2. H_2 -TPR traces of (a) Ni-SMM-0F, (b) Ni-SMM-0.18F, (c) Ni-SMM-0.9F, (d) Ni-SMM-1.8F and (e) Ni-SMM-3.6F. The dashed line is the trace for Pd/Ni-SMM-1.8F. The dotted line represents the temperature.

resulting in mixed dioctahedral-trioctahedral clays [13,16]. Elemental analysis shows that the F content of the samples increases with increasing gel F content. The F content of SMM is lower than that of Ni-SMM-0.18F, despite the higher F content of the gel used to prepare SMM. The relatively high F content of Ni-SMM-3.6F is due to the precipitation of AlF_3 . On the other hand, the Al content of the Ni-SMM clays decreases with increasing gel F content. We explain this by the higher solubility of Al and Ni fluorides compared with the corresponding hydroxides. At low gel F content, part of the Ni and Al ions precipitate as their hydroxides. These hydroxides will be converted to NiO and alumina upon calcination. Hydroxides precipitation competes with the relatively slow formation of the clay. Accordingly, we can relate the higher crystallinity of the final clay to the higher solubility of Ni^{2+} and Al^{3+} in the presence of F. For Ni-SMM-0.18F, the gel and final Ni/Al ratios are similar, because nearly all Ni and Al was precipitated at the relatively low F content. The final Ni/Al ratio of the more crystalline Ni-SMM-1.8F was higher (1.27) at similar Ni content. The Ni content of the Ni-SMM clays is nearly independent from the gel F content. Thus, Ni-SMM clays synthesized at low F content contain a larger amount of a separate NiO phase compared with materials prepared at high F content.

The BET surface area of Ni-SMM decreases with the F content of the gel with the exception of Ni-SMM-3.6F. The surface areas of the well-crystallized SMM sample and Ni-SMM-1.8F are close to values reported for beidellite [45]. The higher surface areas of the Ni-SMM materials prepared at lower F content can be attributed to an increasing amount of alumina, although the differences could in principle also relate to changes in the platelet stacking. The presence of such impurity phases at low F content is corroborated by SEM images (ESI, Fig. S1). The origin of the high surface area of Ni-SMM-3.6F is unclear but could relate to the precipitated AlF_3 . Whereas Ni-SMM-1.8F mainly consists of large clay particles, these particles are also seen for Ni-SMM-0.18F, yet covered by a large number of small rod-like crystallites, which are presumably γ -alumina.

The TPR profiles in Fig. 2 show that the Ni^{2+} species in Ni-SMM can be reduced. Compared with bulk NiO which reduces around 300°C [46], the reduction of the octahedral Ni ions in the SMM structure occurs at much higher temperatures ($650\text{--}800^\circ\text{C}$). The TPR traces for Ni-SMM-0.18F, Ni-SMM-0.9F and Ni-SMM-1.8F have similar shapes. A small portion of Ni^{2+} can be reduced already at temperatures below 500°C . The amount of easily reducible Ni^{2+} ions decreases with increasing crystallinity of the clay phase. It is thus likely that the reduction feature relates to the separate NiO phase on alumina, although we cannot exclude that the Ni ions at the edges of the clay platelets can also be reduced under these conditions. For Ni-SMM-3.6F, the reduction feature extended to higher temperatures, which might have to do with the presence of AlF_3 covering surface Ni sites. The TPR trace of Pd/Ni-SMM-1.8F shifted

to slightly lower temperatures compared with Ni-SMM-1.8F. The shift is likely due to the spillover of H atoms from the reduced Pd phase.

As we will use Ni-SMM as the acidic component for hydroisomerization catalysts (*vide infra*), we also characterized pre-reduced Pd-containing Ni-SMM-1.8F by XRD. Reduction was carried out in the same way as done prior to activity testing (reduction in H_2 flow at 440°C and 35 bar H_2). The Pd loading was 1.0wt%. Ni-SMM-1.8F was chosen, because it is the most active catalyst. Reduction of Pd/Ni-SMM-1.8F led to some structural changes (ESI, Fig. S2). Reflections at 44.3° and 50.7° belong to metallic Ni particles [47]. The more intense reflection at 43.5° is due to NiO. As this feature was not present in the XRD pattern of the parent calcined clay, we infer that the NiO particles most likely originate from reoxidation of the metallic Ni particles formed during reduction. The metallic Ni reoxidized despite measures to protect the reduced sample from air exposure by working in a glove box and covering the XRD sample holder with a Kapton foil. After removal of the Kapton foil (ESI, Fig. S2c), it can be seen that the XRD reflections originating from the clay were less intense, suggesting that the clay structure was partially damaged. The XRD patterns of Pd/Ni-SMM-1.8F did not contain reflections due to metallic Pd, which indicates that Pd was present as very small nanoparticles.

The reduction of Pd/Ni-SMM-1.8F was also investigated by XPS. Initial measurements in which Pd/Ni-SMM-1.8F was reduced in a quartz reactor and then transferred via a glove box to the XPS apparatus using an air-tight transfer holder did show any reduced Ni. In an experiment involving the reduction of Pd/Ni-SMM-1.8F in a reaction cell directly attached to the XPS apparatus, evidence for Ni^{2+} reduction was found. Fig. 3 shows the relevant XPS spectra in the Ni 2p region. The spectrum of fresh Pd/Ni-SMM-1.8F contains a strong feature at 857.4 eV due to Ni^{2+} in close proximity to strong electron-withdrawing F groups. These species are most likely part of the Ni-SMM structure. There is only a small amount of Ni^{2+} in a pure oxidic environment with a binding energy of 854.2 eV. The peak at 863.2 eV is the satellite of the Ni^{2+} feature at 857.4 eV. After reduction, a new feature is observed at 852.7 eV, which is due to metallic Ni. We estimate that about 15% of the Ni ions in the sample were reduced. It should be reminded that XPS is sensitive to the surface of the solids, so that we expect that the overall reduction degree of Ni^{2+} in the structure of the relatively large clay platelets is lower than this value. Assuming that the Ni^{2+} species in close proximity to F are exclusively part of the Ni-SMM structure, the XPS data indicate that the F/Ni ratio in the SMM structure is about 0.6. After reduction, this ratio is 1.2, which may be due to the agglomeration of the reduced Ni ions that were initially highly dispersed in the surface region of the Ni-SMM clay.

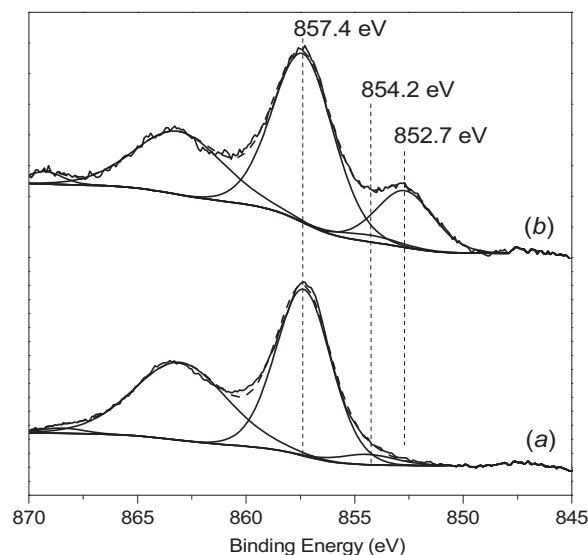


Fig. 3. Ni $2p_{3/2}$ XPS spectra of Pd/Ni-SMM-1.8F before (a) and after (b) reduction in H_2 at 440°C and 1 bar for 16 h.

In order to establish whether Ni^+ ions may be formed during reduction in the hydroxyl-rich environment of the octahedral layer, we carried out *in-situ* EPR measurements for calcined and reduced Ni-SMM-1.8F and Pd/Ni-SMM-1.8F. We report here only the data for Ni-SMM-1.8F, because the data for the reduced Pd-containing clay were very similar (see the Supporting information). The EPR spectrum of calcined Ni-SMM-1.8F shows very weak narrow signals at $g' = 4.3$ (Fig. 4a). This is characteristic for single Fe^{3+} sites. Such signals are frequently observed for single Fe^{3+} located on Si framework positions in aluminosilicates. They might arise from an impurity of the silica source. Note that such materials almost always contain small traces of Fe^{3+} impurities. When such sites are not isolated but form clusters, they usually give rise to a broad line around $g' = 2$, which can also be observed in Ni-SMM-1.8F. In any case, the intensity of these signals is almost negligible compared to the intensity of the reduced sample. The latter one is characterized by strong broad lines, which are typical for ferromagnetic Ni^0 particles (Fig. 4b) [48]. For large bulk Ni particles with extended ferromagnetic domains, an isotropic signal at $g' = 2.3$ is usually observed. When the particles are small and/or ferromagnetic order is established in anisotropic domains, the signals can be very anisotropic at low temperature. Usually, anisotropy is reduced with rising temperature due to thermal spin mobility. Such effects can be observed, too, in Fig. 4. Apart from the fact that the signal intensity is slightly higher after reduction at 550°C , which suggests

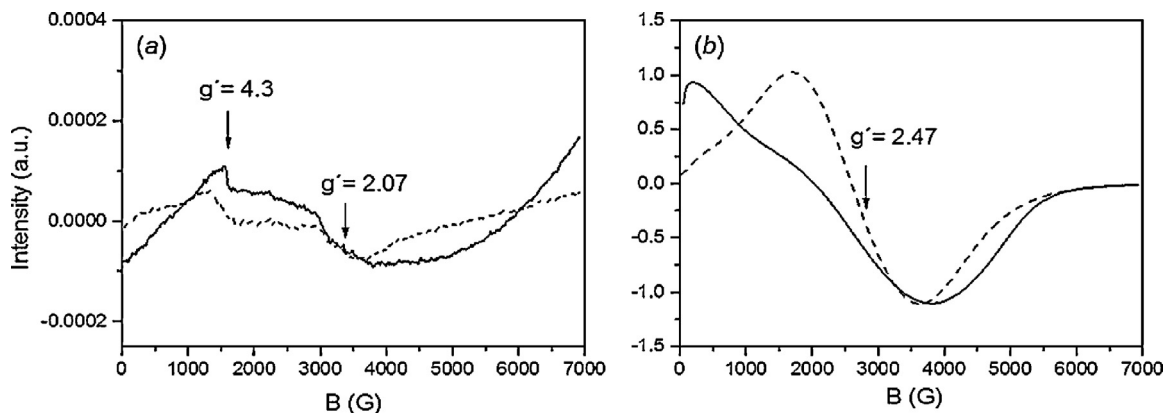


Fig. 4. EPR spectra of (a) calcined and (b) reduced Ni-SMM-1.8F; reduction was done at 550°C . Spectra were recorded at 100 K (full line) and room temperature (dashed line).

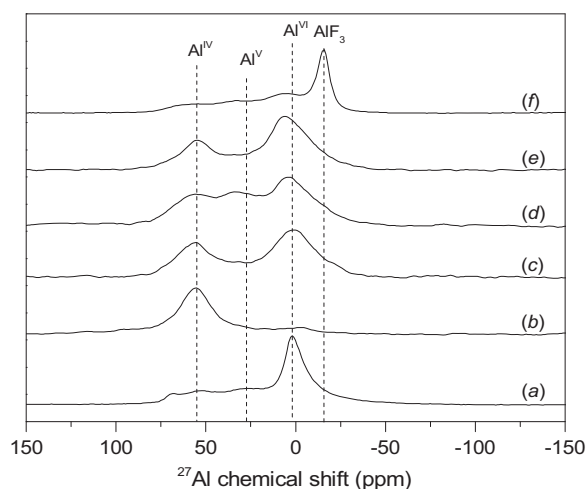


Fig. 5. ^{27}Al MAS NMR of hydrated samples (a) SMM, (b) Ni-SMM-0F, (c) Ni-SMM-0.18F, (d) Ni-SMM-0.9F, (e) Ni-SMM-1.8F and (f) Ni-SMM-3.6F.

that Ni^0 particle formation may be slightly more pronounced, there is not much difference in the EPR spectra after reduction at 550°C (ESI, Fig. S3). In none of the samples, there is any indication for the presence of single Ni^+ sites. Even in the presence of ferromagnetic Ni^0 such sites should be visible at liquid nitrogen temperature, as they show much narrower signals [49].

The ^{27}Al MAS NMR spectra in Fig. 5 show the Al coordination in SMM and Ni-SMM clays. The spectrum of SMM contains peaks due to octahedrally coordinated Al around 0 ppm and two peaks in the 53–68 ppm region, one dominant one at 53 ppm and a weaker one at 68 ppm, which belong to tetrahedrally coordinated Al. The signal at 53 ppm is due to Al in the tetrahedral silica sheets of the SMM clay. The feature at 27 ppm points to five-coordinated Al. The Ni-containing SMM samples display a substantial lower ^{27}Al signal than SMM (Table S1). The Al signal determined in the sample without fluoride (Ni-SMM-0F) decreased by almost one order of magnitude compared with SMM. The decrease of the Al signal is caused by the proximity of the magnetic Ni nuclei. Therefore, we cannot make quantitative statements about the Al coordination in the Ni-SMM clays. Nevertheless, the absence of octahedral Al in Ni-SMM-0F indicates that its octahedral layer is mainly occupied by Ni^{2+} . With increasing F gel content, the contribution of octahedral Al atoms increases as does the Al visibility. It suggests that the average distance between the Al and Ni nuclei increased due to increasing Al and decreasing Ni occupation of the octahedral sites in the SMM structure. It is also seen that a significant part of the NMR-visible Al in Ni-SMM-3.6F is due to AlF_3 .

Table 2
Catalytic activity of reduced Pd-loaded aluminosilicates in the hydroconversion of *n*-heptane ($P_{\text{H}_2} = 35$ bar; molar H_2/alkane ratio = 24).

Catalyst	T_{40} ($^\circ\text{C}$)	E_{act} (kJ/mol)	k/k_{ref}
Ni-SMM-0F	282	157	0.01
Ni-SMM-0.18F	226	128	0.7
Ni-SMM-0.9F	211	126	2.2
Ni-SMM-1.8F	206	128	3.4
Ni-SMM-3.6F	230	126	0.5
SMM	374	152	<0.001
H-USY ^a	233	128	0.4
H-ZSM-5 ^b	221	159	1.0
Silica-alumina ^c	326	120	0.001
Al-SBA-15 ^d	307	135	0.003

^a Ultrastabilized Y (H-USY) with SAR = 9.3.

^b H-ZSM-5 with SAR = 40.

^c Amorphous silica-alumina prepared by co-gelation method with SAR = 19 [17].

^d Al-containing SBA-15 [46].

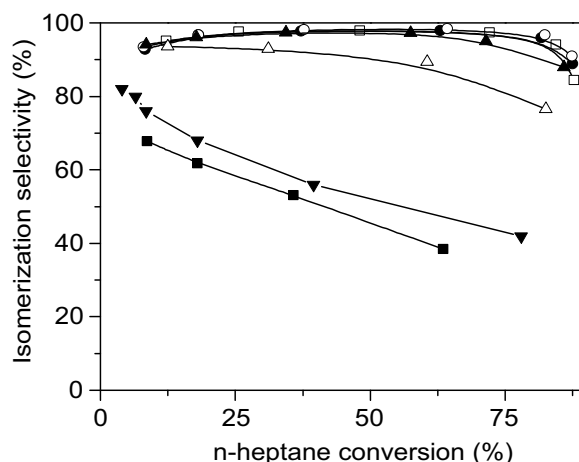


Fig. 6. Isomerization selectivity during *n*-heptane hydroisomerization: (■) Pd/Ni-SMM-0F, (□) Pd/Ni-SMM-0.18F, (●) Pd/Ni-SMM-0.9F, (○) Pd/Ni-SMM-1.8F and (▲) Pd/Ni-SMM-3.6F, (▼) Pd/H-ZSM-5 and (△) Pd/H-ZSM-5 nanosheet.

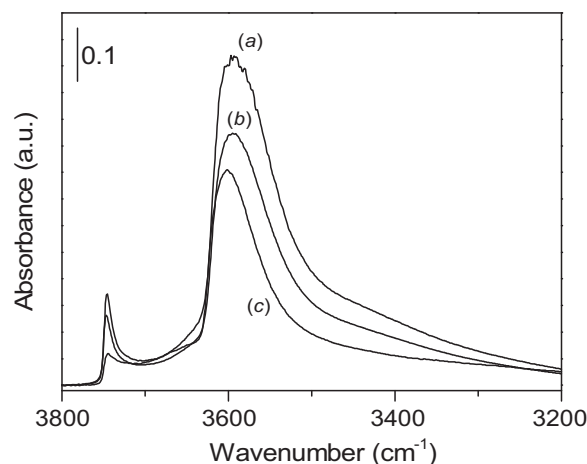


Fig. 7. OH stretch regions of the IR spectra of (a) Ni-SMM-1.8F, (b) reduced Ni-SMM-1.8F and (c) Pd/Ni-SMM-1.8F (reduction in H_2 at 440°C and 1 bar for 16 h).

3.1.1. Catalytic activity measurements

Before characterizing the acidity of these clays, we evaluate their performance in the acid-catalyzed hydroisomerization of *n*-heptane. The SMM and Ni-SMM materials were loaded with 1.0wt% Pd for this purpose. Elemental analysis confirmed that the Pd loading was $1.1 \pm 0.1\text{wt}\%$ for all catalysts. The mechanism of paraffin hydroisomerization involves the dehydrogenation of alkanes to intermediate olefins, isomerization of the intermediate olefins catalyzed by BAS and hydrogenation of these olefins to iso-alkanes [50]. The (de) hydrogenation reactions are catalyzed by Pd. When the goal is to improve the octane number of gasoline, cracking of the intermediate olefins is undesired. The extent of β -scission is limited by operating at not too high temperature and isomerization conversion. When sufficient metal is present, the (de) hydrogenation reactions of alkanes/alkenes are equilibrated. As a consequence, the reaction rate is controlled by the acid-catalyzed conversion of the intermediate olefins [19]. The results of the catalytic tests are presented in Table 2. The activities of Ni-SMM and other solid acids are compared with the activity of a H-ZSM-5 reference zeolite. The activities of the Pd/Ni-SMM catalysts strongly correlate with the crystallinity of the clay, with the exception of Ni-SMM-3.6F that displayed the lowest activity. Compared with the Ni-containing clays, Pd/SMM had a very low activity. All of the Ni-SMM materials were more acidic than the two amorphous silica-alumina materials listed

in Table 2. The catalytic activities of ultrastabilized faujasite (H-USY, steam-calcined zeolite Y, silica-to-alumina ratio (SAR)=9.3) and H-ZSM-5 (SAR=40) were comparable with the activity of Ni-SMM-0.18F. Ni-SMM-1.8F was three times more active than H-ZSM-5 and nearly an order of magnitude more active than the H-USY zeolite.

In alkane hydroisomerization, the selectivity for the intermediate isomerized products is high and may be expected not to change too much if the acid-catalyzed reaction is limiting the reaction rate [11]. When the rate is limited by the metal function, one will find low selectivity to iso-heptanes. The isomerization selectivities (selectivity to iso-heptanes vs. cracked products) are compared for the various catalysts in Fig. 6. Data are included for *n*-heptane conversion levels below 90%. Above this conversion, the isomerization selectivity was very low. Except for Ni-SMM-0F and Ni-SMM-3.6F, the isomerization selectivities of the Pd/Ni-SMM catalysts were always higher than 95%. These results indicate that the Pd/Ni-SMM samples behave like nearly ideal bifunctional catalysts with sufficient metal activity to balance the high acidity of Ni-SMM. Qualitatively, these conclusions are consistent with earlier data reported by Shell for *n*-decane hydroisomerization on Pt/Ni-SMM catalysts [11,16]. The selectivities of our Pd/Ni-SMM catalysts are substantially higher than those of Pd/H-ZSM-5 and Pd/H-USY (note that these catalysts contain the same amount of Pd). For comparison, we included the isomerization selectivity data of a nanostructured Pd/H-ZSM-5 catalyst [51]. The reduced diffusion length in such sheet-like H-ZSM-5 crystals results in much higher isomerization selectivities in comparison with bulk H-ZSM-5. Thus, the ideal bifunctional behavior of the Pd/Ni-SMM hydroisomerization catalysts can be related to the absence of diffusion limitations of alkene intermediates between the acid sites and the Pd function in the clay-based catalysts.

3.1.2. Acidic properties of Ni-SMM and SMM

The acidity of the SMM and Ni-SMM samples was investigated by IR spectroscopy. We will compare spectra of calcined and reduced samples to determine the effect of Ni reduction on the acidity. Reduction was carried out in the environmental IR cell in flowing hydrogen at 440 °C and 1 bar for 16 h. As an example, Fig. 7 shows IR spectra of the hydroxyl region of Ni-SMM-1.8F before and after reduction and the corresponding data for reduced Pd/Ni-SMM-1.8F. The broad and intense band around 3600 cm⁻¹ is due to structural OH groups coordinating to the octahedral cations in the SMM structure. Reduction leads to a decrease of the intensity of this band. The decrease is slightly more pronounced for the Pd-containing sample. It is caused by the reduction of part of the octahedral Ni²⁺ in the SMM structure, which leads to the removal of OH groups as water. The intense band due to these structural OH groups makes direct investigation by IR spectroscopy of acidic bridging OH groups that resonate in the same region impossible. Accordingly, we make use of pyridine and CO as basic probes and also employ the selective isotopic exchange of the most acidic OH groups with deuterated benzene (C₆D₆) to study the complicated acidity situation in these clays.

Pyridine IR was used to probe BAS and Lewis acid sites (LAS). Relevant spectra are shown in the Supporting Information (ESI, Fig. S4). These spectra were deconvoluted in the usual way into bands due to BAS (1546 cm⁻¹) and LAS (1451 cm⁻¹). The acid site densities for Ni-SMM-1.8F are given in Table 3. For the calculation of these densities, the extinction coefficients reported by Datka et al. were used [52]. It is seen that the samples contain much more LAS than BAS. Reduction of the sample results in an increasing amount of BAS at the expense of LAS. These changes can be related to the reduction of Ni²⁺ ions in the interlayer. These results are in good agreement with earlier reported data [11]. Importantly, the amount of strong BAS as represented by the intensity of the 1546 cm⁻¹ band after

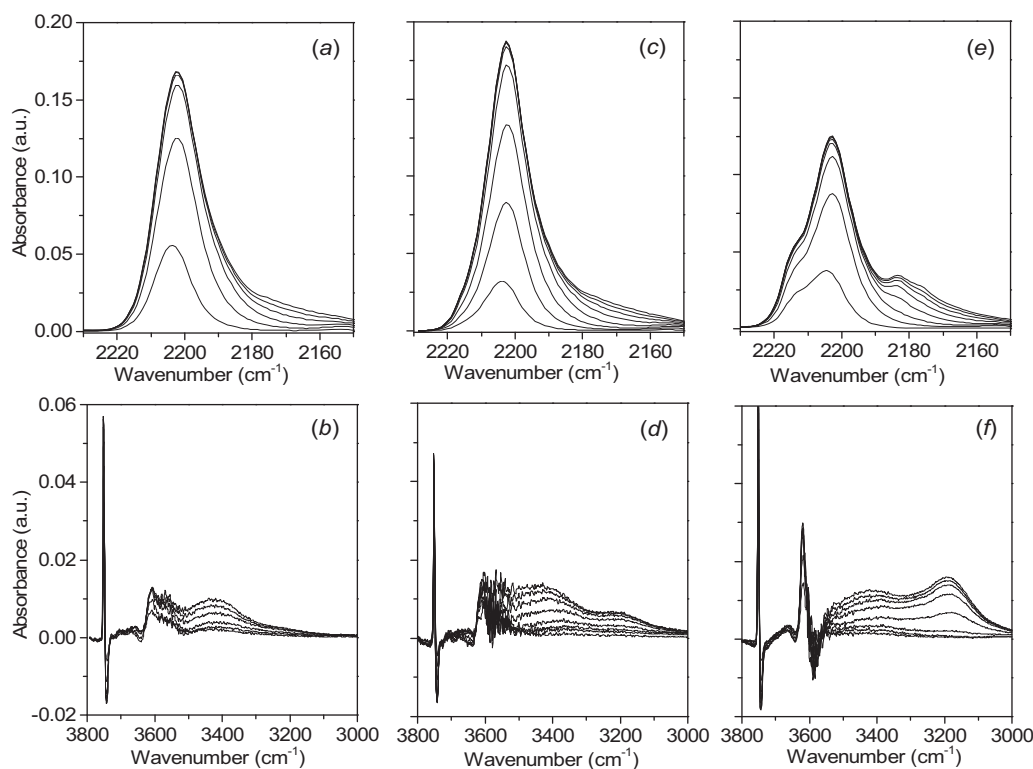


Fig. 8. IR spectra of CO adsorbed at -183°C on (a, b) Ni-SMM-0.18F, (c, d) Ni-SMM-0.9F and (e, f) Ni-SMM-1.8F. The top and bottom spectra are of the carbonyl and hydroxyl stretching regions, respectively.

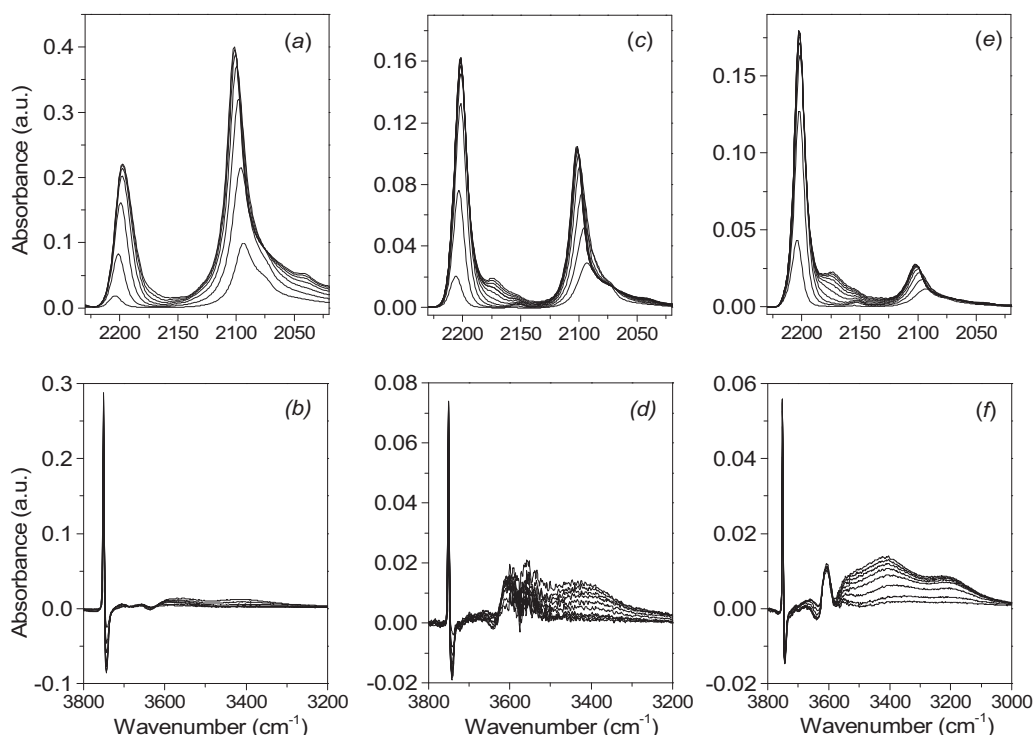


Fig. 9. IR spectra of CO adsorbed at -183°C on reduced Ni-SMM samples (reduction in H_2 at 440°C and 1 bar for 16 h): (a, b) Ni-SMM-0F, (c, d) Ni-SMM-0.18F and (e, f) Ni-SMM-0.9F.

Table 3

Acid site density determined by IR spectroscopy of adsorbed pyridine for Ni-SMM-1.8F before and after reduction (reduction in H_2 at 440°C and 1 bar for 16 h).

Pretreatment	$T_{\text{evacuation}} (^{\circ}\text{C})$	BAS ($\mu\text{mol/g}$)	LAS ($\mu\text{mol/g}$)
Calcination	150	158	1195
	200	117	1014
	300	100	549
	400	77	309
Reduction	150	220	962
	200	224	769
	300	141	354
	400	65	204

evacuation at 400°C did not change appreciably upon reduction of Ni-SMM-1.8F. This suggests that reduction of part of the Ni cations does not affect the strong BAS in Ni-SMM.

IR spectra for the Ni-SMM materials as a function of the CO coverage until saturation are given in Figs. 8–10. For the calcined samples (Fig. 8), the CO stretch region of the spectra is dominated by an intense band at 2202 cm^{-1} due to LAS. Ni-SMM-1.8F contains an additional shoulder at 2212 cm^{-1} . At higher CO coverage, a band at 2183 cm^{-1} with a shoulder at 2175 cm^{-1} appears due to acidic OH groups of different strengths. In the OH stretch region, the band at 3430 cm^{-1} is due to perturbation of acidic OH groups by CO. The band below 3200 cm^{-1} is due to perturbation of stronger acidic OH groups. The latter band can also be seen with much weaker intensity in the spectra for Ni-SMM-0.9F. The large shift in the OH frequency implies that it is associated with strong acidic OH groups. These BAS are related to the 2183 cm^{-1} feature in the CO region.

The CO_{ads} IR spectra of the reduced Ni-SMM samples are pronouncedly different (Fig. 9). We included here reduced Ni-SMM-0F to exemplify the large amount of reduced Ni formed in this sample. The spectra of the reduced Ni-SMM-0F are dominated by bands at 2195 and 2100 cm^{-1} . The intensity of the 2202 cm^{-1} band observed for the calcined samples is strongly decreased during the reduction treatment. The band at 2100 cm^{-1} is due to CO coordi-

nating to metallic Ni [53]. The band at 2195 cm^{-1} is due to relatively weak Lewis acidic Al^{3+} sites. We suspect that the 2195 cm^{-1} band is not visible in the CO_{ads} IR spectra of the calcined samples, because it is masked by the strong band due to CO adsorbed to Ni^{2+} . In the OH region, the negative band at 3745 cm^{-1} is due to CO adsorption on weakly acidic silanol groups neighboring Lewis acid Al^{3+} sites. CO adsorption on these silanol groups gives rise to relatively weak silanol perturbation (band at 3607 cm^{-1}). All of these features are also observed in the spectra for reduced Ni-SMM-0.18F and Ni-SMM-0.9F. With increasing gel F content, it is seen that the amount of Ni metal decreases. This is in keeping with our earlier conclusion that more Ni^{2+} is located in the SMM structure, which cannot be reduced at 440°C according to TPR. Thus, the higher Ni metal content in reduced Ni-SMM-0F stems from the larger amount of free bulk NiO in this sample. For reduced Ni-SMM-0.18F, a weak feature at 2175 cm^{-1} is observed that shifted to 2173 cm^{-1} with increasing CO coverage. It points to the presence of BAS. As this band was not observed in calcined Ni-SMM-0.18F, we speculate that reduction of Ni^{2+} ions at cation exchange position of the clay occurred [17]. The position of the perturbed hydroxyl band (3412 cm^{-1}) indicates that the resulting BAS are of weak strength. The spectra of reduced Ni-SMM-0.9F carry evidence for the presence of strong BAS in the form of the perturbed OH feature at 3200 cm^{-1} and a CO stretch feature at 2183 cm^{-1} . The spectra for reduced Ni-SMM-3.6F (not shown) are similar, except that the intensity of the strongly perturbed hydroxyl band is weaker and there is no reduced Ni in this sample. In line with this, Ni-SMM-3.6F is the only sample in the set of Ni-SMM materials that retains the Lewis acid related band above 2200 cm^{-1} upon reduction.

Next, we compare CO_{ads} IR spectra for reduced Ni-SMM-1.8F and Pd/Ni-SMM-1.8F after the first CO dose, after the fifth CO dose and after saturation of the sample in Fig. 10. The band due to Ni^{2+} at 2202 cm^{-1} is less intense for reduced Pd/Ni-SMM-1.8F because of deeper reduction of NiO. Due to the presence of Pd metal, the band at 2100 cm^{-1} is more intense and broadened for Pd/Ni-SMM-1.8F. At higher CO coverage, bands related to the acidic hydroxyl

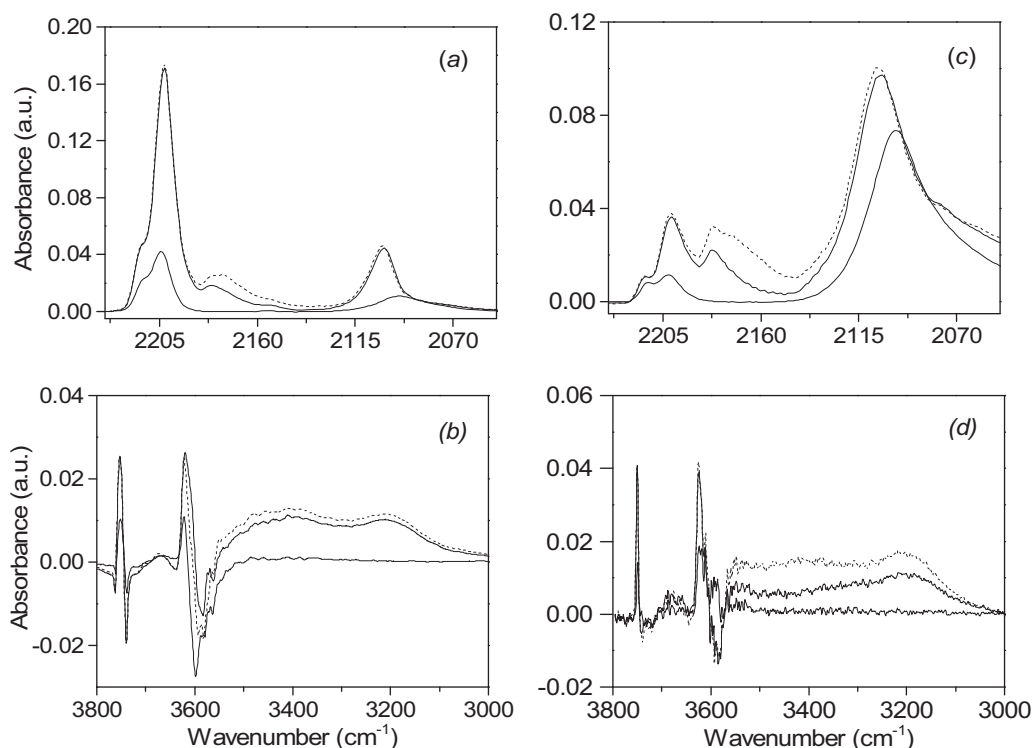


Fig. 10. CO and hydroxyl OH regions of the IR spectra of CO adsorbed at -183°C on (a, b) reduced Ni-SMM-1.8F and (c, d) reduced Pd/Ni-SMM-1.8F. Reduction was carried out in flowing H_2 at 440°C for 16 h.

groups in the region $2175\text{--}2185\text{ cm}^{-1}$ appear. The intensity is similar for both samples, although the band is broader for reduced Pd/Ni-SMM-1.8F. The broadening points to heterogeneity in the acid site distribution. The presence of various types of BAS is also evident from the bands around 3400 cm^{-1} and 3200 cm^{-1} in the OH region of the spectra.

The acid strength of OH groups in zeolites, clays and amorphous silica-alumina materials can be discriminated by the shift in the OH stretching frequency upon CO adsorption [54,55]. Table 4 summarizes the positions of the bands belonging to different BAS in Ni-SMM in the CO and perturbed OH region and literature data for zeolites and amorphous silica-alumina. The Ni-SMM samples contain at least two types of acidic OH groups that give rise to CO bands at 2175 and 2184 cm^{-1} . Based on earlier investigations [18,56], the band at 2184 cm^{-1} represents the more strongly acidic OH population. Detailed inspection of the corresponding OH region for reduced Ni-SMM-1.8F and reduced Pd/Ni-SMM-1.8F shows that the appearance of the most strongly perturbed OH feature at 3216 cm^{-1} correlates with the negative feature at 3592 cm^{-1} . The OH shift of 374 cm^{-1} is at the high end of shifts reported for strongly acidic sites in USY zeolites, which suggests that Ni-SMM contains a small fraction of very strong BAS. From the CO_{ads} IR spectra, it is not clear to which unperturbed OH vibration the 2175 cm^{-1} belongs. Below, we will show that it is most likely related to a feature around 3644 cm^{-1} . The lower acidity of these OH groups is consistent with the smaller OH shift ($<300\text{ cm}^{-1}$) upon CO perturbation. The CO_{ads} IR data clearly point out that Ni-SMM clay contains two types of strong BAS, characterized by OH stretching frequencies of 3644 cm^{-1} and 3592 cm^{-1} .

It has been earlier demonstrated that the protons in acidic OH groups can be selectively exchanged for deuterium by contacting the sample with C_6D_6 . Haw and co-workers followed the H/D exchange process of OH groups in zeolites with C_6D_6 with ^1H NMR spectroscopy [57]. Recently, IR spectroscopy was employed to follow the same exchange process in a range of acidic aluminosilicates

[18]. Even small amounts of strong BAS in aluminosilicates containing a wider range of OH groups as encountered in steam-stabilized Y zeolites, clays and amorphous silica-alumina can be distinguished and quantified in this way. Fig. 11 displays the IR spectra of the progressive isotopic H/D exchange of calcined and reduced Ni-SMM-0.18F. At the shortest contact time at 30°C , a single band at 2682 cm^{-1} appears in the OD stretching region. It relates to the exchange of the most acidic OH groups in this sample. With increasing isotopic exchange, other OH groups appear, namely a band at 2637 cm^{-1} and a broad background. By comparison of these spectra with the OH region of the freshly dehydrated clay, we can conclude that the isotopic exchange of Si-OH, Al-OH and Ni-OH groups was very low. When the isotopic exchange was carried out at higher temperatures, the bands at 2637 cm^{-1} and 2682 cm^{-1} are masked by the strong band due to structural OD groups. The results are qualitatively similar for the calcined and reduced Ni-SMM-0.18F samples.

Fig. 12 compares the spectra after isotopic H/D exchange of Ni-SMM-1.8F and reduced Ni-SMM-1.8F. Already after the shortest exchange time at 30°C , the spectra contain the two bands at 2637 cm^{-1} and 2682 cm^{-1} also seen for Ni-SMM-0.18F. The bands are much more intense in Ni-SMM-1.8F. With increasing isotopic exchange temperature, the stronger background signal masks the bands at 2637 cm^{-1} and 2682 cm^{-1} . The intensities of these bands are comparable for calcined and reduced Ni-SMM-1.8F, suggesting that the reduction treatment did not increase the BAS content. The OD stretching frequencies of 2637 cm^{-1} and 2682 cm^{-1} can be correlated to OH stretching frequencies of 3592 cm^{-1} and 3644 cm^{-1} , respectively. As it is reasonable to assume that the BAS characterized by the band at 3592 cm^{-1} cause the strong acidity of the Ni-SMM clays, we determined their concentration from IR spectra after exchange at 50°C using the method detailed in literature [17]. In this way, we found that Ni-SMM-1.8F and reduced Ni-SMM-1.8F contain approximately $11\text{ }\mu\text{mol/g}$ strong BAS. The concentration of

Table 4Infrared band positions of OH(D)··CO complexes in the CO stretch region on Ni-SMM samples after adsorption of a small dose of CO.^a

Sample	State	CO _{ads} IR before H/D exchange		CO _{ads} IR after H/D exchange
		ν_{CO} (cm ⁻¹)	$\Delta\nu_{\text{OH}}$ (cm ⁻¹)	$\Delta\nu_{\text{OD}}$ ($\Delta\nu_{\text{OHcalc}}$) (cm ⁻¹)
Ni-SMM-0F	Reduced	2173	227	n.d
Ni-SMM-0.18F	Calcined	2184	~244	165 (224)
	Reduced	2173	n.d.	168 (228)
		2184	330	226 (307)
Ni-SMM-0.9F	Calcined	2175	~250	161 (219)
		2184	374	220 (299)
	Reduced	2173	~250	165 (224)
		2183	360	235 (320)
Ni-SMM-1.8F	Calcined	2176	~253	167 (227)
		2183	384	266 (361)
	Reduced	2175	~255	163 (221)
		2180	374	252 (343)
Ni-SMM-3.6F	Reduced	2176	~256	180 (219)
		2182	n.d.	251 (341)

^a The shifts in the hydroxyl region $\Delta\nu_{\text{OH}}$ are relative to OH band around at 3644 cm⁻¹ and 3592 cm⁻¹. The shifts in the OD region $\Delta\nu_{\text{OD}}$ are relative to OD band at 2682 cm⁻¹ and 2637 cm⁻¹, after progressive selective H/D exchange with C6D6 at 50 °C.

such sites reduced Ni-SMM-0.18F and Ni-SMM-0.9F is much lower, namely 1.4 $\mu\text{mol/g}$ and 2 $\mu\text{mol/g}$, respectively.

Before resolving the intrinsic acidity of the BAS in Ni-SMM, we briefly discuss IR spectra for SMM (ESI, Figs. S5 and S6). Figs. S5a and S5b, respectively, show the CO_{ads} and Py_{ads} IR spectra for SMM. The CO_{ads} IR spectra contain a strong band at 2177 cm⁻¹ due to acidic hydroxyl groups. This feature relates to BAS and has earlier been observed in other clays such as saponites and also in amorphous silica-alumina [19]. The Py_{ads} IR spectra show that this material contains a small amount of BAS; their strength is lower than of the BAS in Ni-SMM. Relevant H/D exchange IR spectra are shown in Fig. S6. After H/D exchange at 50 °C and 150 °C, two weak bands at 2754 cm⁻¹ and 2682 cm⁻¹ are visible for SMM. Different from the Ni-SMM materials, there is no band around 2637 cm⁻¹. This supports the conclusion that the strong acid sites in Ni-SMM relate to the presence of Ni in the structure.

3.1.3. Intrinsic acidity of the acid sites

The significantly higher catalytic activity of Ni-SMM-1.8F in alkane hydroisomerization compared with H-ZSM-5 and H-USY zeolite appears to be linked to a relatively small amount of strong acid sites in the clay (11 $\mu\text{mol/g}$). The H-ZSM-5 and H-USY reference materials contain BAS in amounts of 530 $\mu\text{mol/g}$ [47] and 167 $\mu\text{mol/g}$ [18], respectively. Accordingly, it is interesting to probe the intrinsic acidity of the BAS in Ni-SMM. We employed CO_{ads} IR spectroscopy to determine the acidity of the OD groups in reduced Ni-SMM after H/D exchange at 50 °C. The relevant spectra for Ni-SMM-0.9F and Ni-SMM-1.8F are shown in Fig. 13. We will discuss the appearance of bands due to CO₂ around 2350 cm⁻¹ below. The OD shift of the band at 2682 cm⁻¹ is about 168 cm⁻¹ ($\Delta\nu_{\text{OH}} = 228 \text{ cm}^{-1}$), corresponding to typical Brønsted acidity of amorphous silica-alumina. For ¹⁸Ni-SMM-0.9F, perturbation of the 2637 cm⁻¹ band results in a band at 2402 cm⁻¹ with $\Delta\nu_{\text{OD}} = 235 \text{ cm}^{-1}$ ($\Delta\nu_{\text{OH}} = 320 \text{ cm}^{-1}$). The BAS in this clay display similar strength as the BAS in H-ZSM-5 ($\Delta\nu_{\text{OH}} \approx 310 \text{ cm}^{-1}$) [18]. For Ni-SMM-1.8F, the $\Delta\nu_{\text{OD}}$ shift of 252 cm⁻¹ corresponds to $\Delta\nu_{\text{OH}} = 343 \text{ cm}^{-1}$. Direct perturbation of the OH stretching band suggests that $\Delta\nu_{\text{OH}} = 374 \text{ cm}^{-1}$. It shows that the optimum Ni-SMM-1.8F material contains the strongest acid sites. The reason for the discrepancy in the OH and OD shifts is the lower mobility and acidity of the deuterium ion, resulting in a smaller shift than can be expected on the basis of the mass difference alone [58]. On the basis of these data, we conclude that the strength of the BAS in Ni-SMM-1.8F can be placed at the high end of the acidity scale of

aluminosilicates; its acidity is similar or slightly higher than that of the strongest acid sites in H-USY zeolite ($\Delta\nu_{\text{OH}} = 300 - 350 \text{ cm}^{-1}$) [49]. The Ni-SMM-3.6F clay also gave rise to similar bands, but the intensity of the most perturbed OD feature is considerably lower. The spectra also show that CO₂ is formed upon exposure of our samples to CO at -183 °C. These features were not seen in the CO_{ads} IR experiments of non-reduced Ni-SMM samples. We tentatively explain this to the presence of very finely dispersed Ni clusters in the reduced sample, which become reoxidized in the IR cell by trace amount of oxygen (the pressure in the cell was lower than 5×10^{-6} mbar). The high reactivity of the reduced Ni phase is in line with the difficulty in keeping reduced Ni in the metallic state by transfer in an air-tight transfer holder to the XPS apparatus. The resulting highly dispersed NiO particles are apparently very reactive and can oxidize CO at temperatures as low as -183 °C.

Fig. S7 shows the ¹H MAS NMR spectra of the SMM and Ni-SMM clays. Quantitative interpretation of the spectra of the Ni-containing clays is hampered by the presence of the magnetic Ni. The ¹H MAS NMR spectrum of SMM exhibit four resonances. The peaks at 1.5 and 2.5 ppm correspond to the structural SiOH and AlOH groups, respectively. The peak at ~7 ppm is assigned to protons with Brønsted acidity and the peak at 4 ppm to remaining intercalated water molecules, after dehydration at 150 °C. The ¹H NMR signal of the structural hydroxyl groups at 2.5 ppm decreased significantly when Ni was present in the clay. Increasing the fluoride content results in a decrease of the amount of structural OH groups, as OH groups are replaced by F in the clay structure. The most interesting feature is the appearance of two resonances in the 10–19 ppm region for the Ni-SMM clays. These features can be most clearly seen in Ni-SMM-1.8F material. Acidic sites with downfield chemical shifts as large as ~13 ppm have been reported for layered metal oxides [59]. Tentatively, the signal at 19 ppm can be assigned to strongly acidic sites present in the Ni-SMM clays.

3.2. Density functional theory calculations

To support the interpretation of the IR data, we investigated the strength of bridging OH groups in the interlayer for beidellite with DFT calculations. We computed the shift of the OH stretch frequency upon adsorption of CO. We carried out such calculations for various types of substitutions of the SMM clay structure. The interlayer surface, which is the (001) termination of the tetrahedral sheet, is contained in the periodic model of beidellite. The dioctahedral beidellite clay model used in these calculations is shown

Table 5
Computed OH stretch frequencies before and after CO adsorption and resulting $\Delta\nu_{\text{OH}}$ as determined by DFT calculations. For the SMM model, substitutions were made in the beidellite $[\text{Al}_4\text{O}_8(\text{OH})_4][\text{Si}_8\text{O}_{12}]$ structure. For the faujasite model, the Si/Al ratio was varied between 2.4 and 47.

Model	Substitution		Formula	ν_{OH} (cm^{-1})		$\Delta\nu_{\text{OH}}$ (cm^{-1})
	T layer	O layer		unperturbed	with CO	
SMM	$1 \times \text{Al}^{3+}$ for Si^{4+}	–	$\text{H}^+[\text{Al}_4\text{O}_8(\text{OH})_4][\text{Si}_7\text{AlO}_{12}]^-$	3760	3293	467
SMM	$1 \times \text{Al}^{3+}$ for Si^{4+}	$1 \times [\text{NiF}]^+$ for $[\text{AlO}]^+$	$\text{H}^+[\text{Al}_3\text{O}_7\text{NiF}(\text{OH})_4][\text{Si}_7\text{AlO}_{12}]^-$	3723	3179	544
SMM	$1 \times \text{Al}^{3+}$ for Si^{4+}	$1 \times \text{or } 2 \times \text{F}^-$ for OH^-	$\text{H}^+[\text{Al}_4\text{O}_8(\text{OH})_3\text{F}][\text{Si}_7\text{AlO}_{12}]^-$	3760	3284	476
			$\text{H}^+[\text{Al}_4\text{O}_8(\text{OH})_2\text{F}_2][\text{Si}_7\text{AlO}_{12}]^-$	3757	3285	472
SMM	$1 \times \text{Al}^{3+}$ for Si^{4+}	$6 \times \text{Ni}^{2+}$ for 4 Al^{3+}	$\text{H}^+[\text{Ni}_6\text{O}_8(\text{OH})_4][\text{Si}_7\text{AlO}_{12}]^-$	3731	3224	507
SMM	$1 \times \text{Al}^{3+}$ for Si^{4+}	$3 \times \text{Ni}^{2+}$ for 2 Al^{3+}	$\text{H}^+[\text{Al}_2\text{Ni}_3\text{O}_8(\text{OH})_4][\text{Si}_7\text{AlO}_{12}]^-$	3745	3265	480
Faujasite	Si/Al = 2.4	–	$\text{H}^+_{14}[\text{Si}_{34}\text{Al}_{14}\text{O}_{96}]$	3766	3395	371
Faujasite	Si/Al = 7	–	$\text{H}^+_{6}[\text{Si}_{42}\text{Al}_6\text{O}_{96}]$	3746	3339	407
Faujasite	Si/Al = 47	–	$\text{H}^+[\text{Si}_{47}\text{AlO}_{96}]$	3739	3205	534

in Fig. 14a. The various substitutions and the computed CO frequencies are given in Table 5 and the corresponding structures are displayed in Fig. 14b and c. It is important to note that DFT overestimates the binding of CO with the consequence that the predicted OH frequency shifts will be higher than observed in the CO_{ads} IR spectra. As this renders our analysis semi-quantitative, we first computed as a reference the shifts for the acid sites located in the supercages of faujasite zeolite as a function of the framework Si/Al ratio. As is well established for zeolites, the proton acidity strongly depends on this ratio. The data for faujasite zeolite Y in Table 5 support this notion. When the framework Al atoms are sufficiently diluted as they are for $\text{Si/Al}_{\text{framework}} = 47$, $\Delta\nu_{\text{OH}}$ equals 534 cm^{-1} . Due to over-binding, these values are considerably higher than experimental values that lie in the range $\Delta\nu_{\text{OH}} = 300 - 350\text{ cm}^{-1}$

for stabilized Y zeolite [49]. It is interesting to point out that the higher end of this range is usually reported for zeolites with enhanced sites, which are presumed to involve the presence of cationic extraframework Al species adjacent to the acid sites.

For the SMM clay, it was found that CO does not adsorb to the structural OH group that coordinates to the octahedral Al ions. Replacement of a tetrahedral Si^{4+} atom by Al^{3+} in beidellite results in a bridging hydroxyl group in the interlayer (Fig. 14b). The computed $\Delta\nu_{\text{OH}}$ of this hydroxyl group upon CO adsorption is 467 cm^{-1} . Thus, the acidity of this proton is slightly lower than that of the supercage protons in faujasite. We then investigated the influence of the introduction of Ni and F in this clay with one tetrahedral substitution. When $[\text{Al}_{\text{octahedral}}-\text{O}]^+$ is replaced by $[\text{Ni}_{\text{octahedral}}-\text{F}]^+$ (Fig. 14c), $\Delta\nu_{\text{OH}}$ is computed to be 544 cm^{-1} , which is higher than the acidity of Y zeolite. This result shows that Ni-F substitution

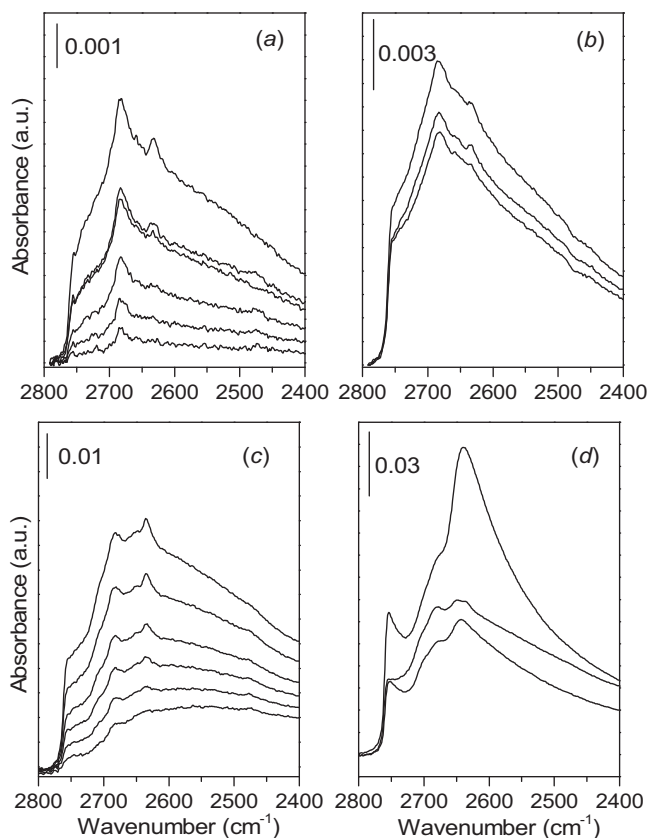


Fig. 11. IR spectra of the OD region after selective isotopic H/D exchange for (a, b) Ni-SMM-0.18F and (c, d) reduced Ni-SMM-0.18F. The spectra are taken after exposure to C_6D_6 at different temperatures and different exposure times. The traces from bottom to top are taken after exposure times of (a, c) 10 s, 30 s, 300 s, 600 s, 1200 s, 1800 s at 30°C and (b, d) for 1800 s at 50°C , 150°C and 250°C .

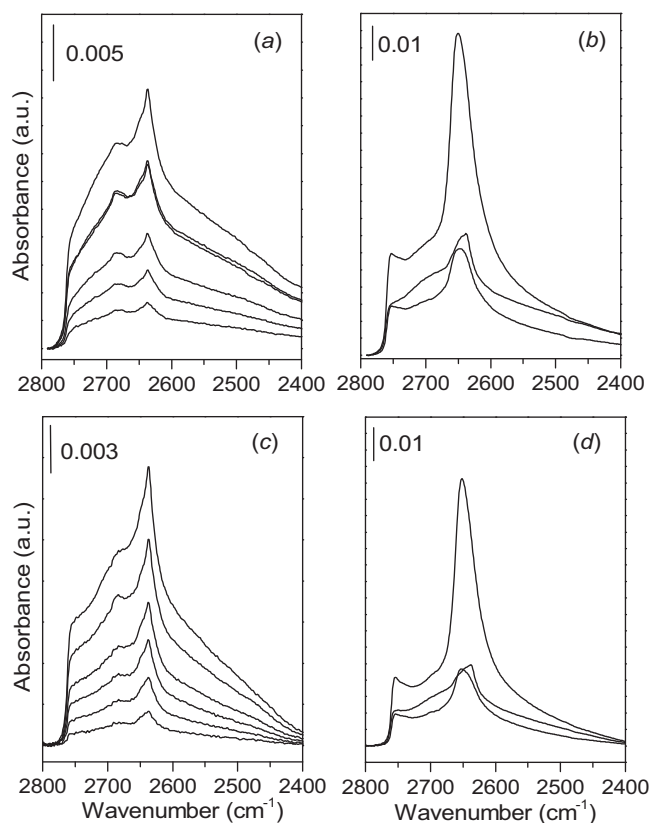


Fig. 12. IR spectra of the OD region after selective isotopic H/D exchange for (a, b) Ni-SMM-1.8F and (c, d) reduced Ni-SMM-1.8F. The spectra are taken after exposure to C_6D_6 at different temperatures and different exposure times. The traces from bottom to top are taken after exposure times of (a, c) 10 s, 30 s, 300 s, 600 s, 1200 s, 1800 s at 30°C and (b, d) for 1800 s at 50°C , 150°C and 250°C .

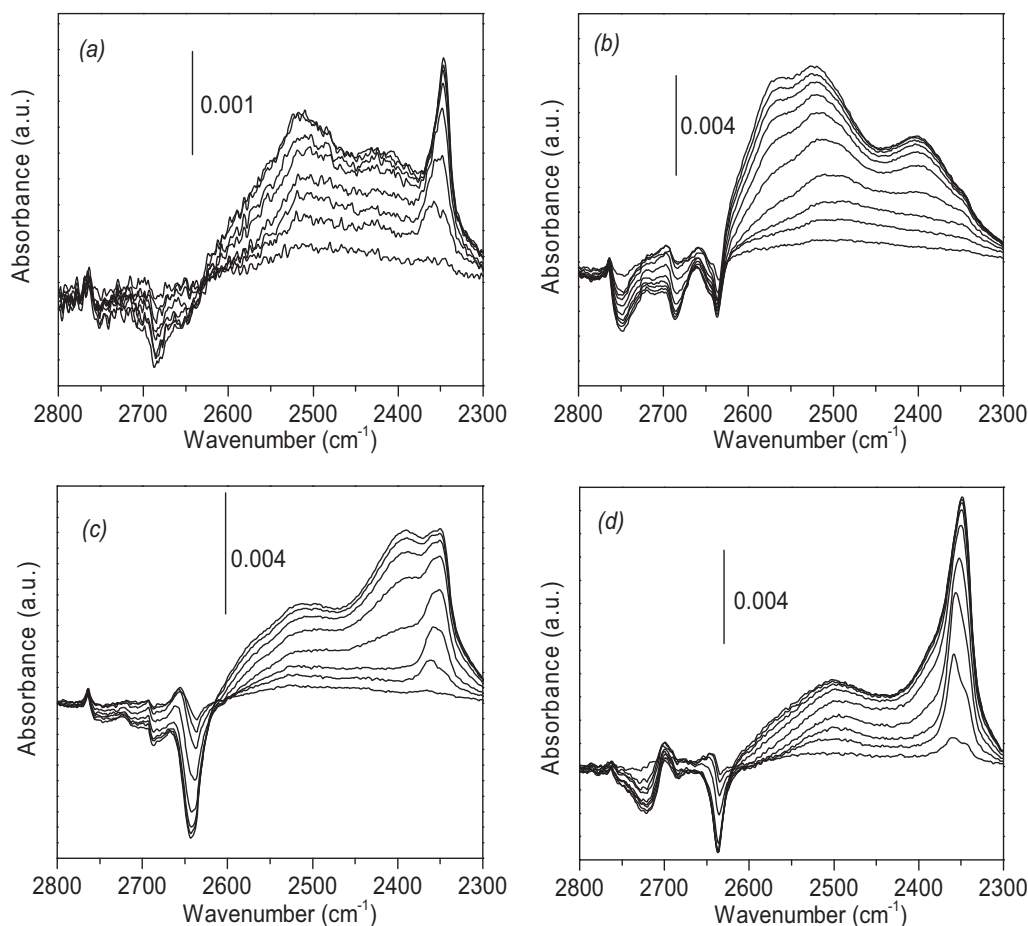


Fig. 13. Infrared spectra upon CO adsorption at -183°C of H/D exchanged Ni-SMM (reduction in H_2 at 440°C and 1 bar for 16 h): (a) Ni-SMM-0.18F, (b) Ni-SMM-0.9F, (c) Ni-SMM-1.8F and (d) Ni-SMM-3.6F.

can lead to enhanced acidity of the interlayer proton. In order to understand the enhanced acidity due to Ni-F introduction in the clay structure, we also investigated the influence of separate Ni^{2+} and F^- introduction in the same SMM model with one substitution in the tetrahedral sheet. F^- ions can only be introduced into the SMM clay structure without simultaneous Ni introduction, when they replace the OH^- group attached to octahedral Al^{3+} . The resulting structures give rise to $\Delta\nu_{\text{OH}}$ values in the range of $472\text{--}476\text{ cm}^{-1}$. This result implies that substituting F for OH in SMM will lead to nearly unchanged acidity of the SMM clay, which is consistent with our experimental results. For the substitution of octahedral Al^{3+} by Ni^{2+} , we considered two models. The first model involves complete substitution of the octahedral layer by Ni^{2+} . This can be achieved by replacing four Al^{3+} in an SMM unit cell by six Ni^{2+} , resulting in complete occupation of the octahedral layer. The resulting trioctahedral clay gives rise to $\Delta\nu_{\text{OH}} = 507\text{ cm}^{-1}$. A mixed configuration with 2 Al^{3+} and 3 Ni^{2+} per unit cell resulted in $\Delta\nu_{\text{OH}} = 480\text{ cm}^{-1}$. Thus, introduction of either Ni^{2+} or F^- in the SMM structure does not affect the acidity of the interlayer BAS. When $\text{Ni}_{\text{octahedral}}\text{-F}$ units replace $\text{Al}_{\text{octahedral}}\text{-O}$ units, the acidity is strongly enhanced. This is due to the electron-withdrawing nature of the F anion in the second coordination shell of the bridging hydroxyl group.

3.3. General discussion

Fluoride anions in the synthesis gel improve the crystallinity of hydrothermally prepared Ni-SMM clay, because fluoride slows down precipitation of Al and Ni hydroxides. After calcination, Ni-

SMM prepared at low gel F content contains a significant fraction of Ni-oxide on γ -alumina in addition to the Ni-substituted SMM clay. When the F content is too high, AlF_3 will precipitate. A well-crystallized, relatively pure Ni-SMM clay was synthesized under hydrothermal conditions (300°C , 40 h) from a gel with a molar composition $1.6\text{ SiO}_2 : \text{Ni}(\text{C}_2\text{H}_3\text{O}_2)_2 \cdot 4\text{H}_2\text{O} : 1.1\text{ Al}(\text{O-}i\text{-Pr})_3 : 2.0\text{ NH}_4\text{F}$. XPS shows that nearly all Ni^{2+} is in close proximity to F, which implies that most of Ni^{2+} is built into the SMM structure. This sample is much more active in *n*-heptane hydroisomerization than SMM prepared with NH_4F and Ni-SMM prepared without NH_4F . Combining the IR characterization and the DFT results, we conclude that SMM and Ni-SMM-0F contain one type of BAS. The acidity relates to Al^{3+} for Si^{4+} substitutions in the tetrahedral layer of SMM clay; the aluminium-occupied Al tetrahedral are connected to aluminium-occupied oxygen octahedra in the octahedral layer of the beidellite structure. The structure of these materials will only contain F^- attached as terminal groups where it replaces OH^- groups. The DFT calculations indicate that the acidity of the interlayer OH group is comparable to or slightly weaker than that of low-silica Y zeolite. Only when F is placed in the second coordination shell of the tetrahedral Al atom, a second type of acid sites arises with enhanced strength as predicted by the DFT calculations. Our findings, therefore, strongly suggest that the replacement of structural O anions bridging by tetrahedral and octahedral cations is only possible by $[\text{Al}^{3+}\text{-O}]^+ \rightarrow [\text{Ni}^{2+}\text{-F}]^+$ substitution in the octahedral layer. The enhanced acidity can be ascribed to the presence of F in the second coordination shell of the proton; Ni^{2+} is required to introduce F in these specific positions.

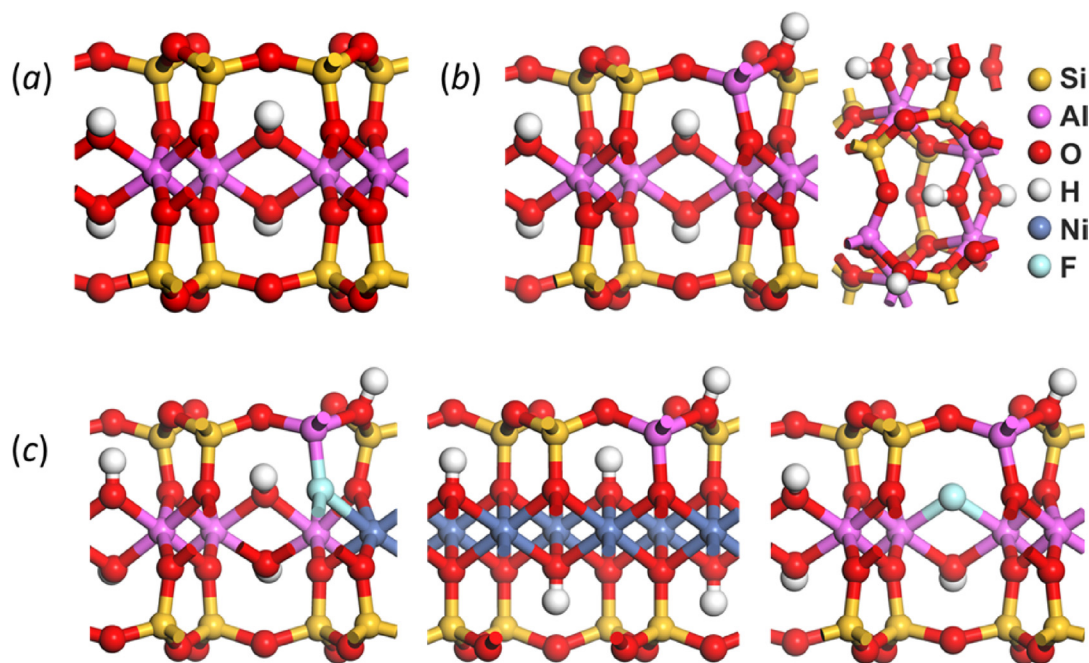


Fig. 14. Structural models of the clays used in periodic density functional theory calculations: (a) neutral beidellite, (b) beidellite structure with one tetrahedral Al^{3+} site and a corresponding hydroxyl group in the interlayer, (c) model for (from left to right) substitution of $[\text{Al}^{3+}\text{-O}]^+ \rightarrow [\text{Ni}^{2+}\text{-F}]^+$ in the octahedral layer, replacement of 4 Al^{3+} by 6 Ni^{2+} in the octahedral layer and substitution of OH in the octahedral layer by F.

We attempted to study the Ni-SMM clay with ^{19}F MAS NMR spectroscopy (ESI, Fig. S8). Although ^{19}F is one of the most sensitive nuclei for NMR study because of its large gyromagnetic ratio and 100% natural abundance, the large amount of magnetic Ni nuclei will also perturb the ^{19}F NMR experiments of the Ni-SMM clays. The ^{19}F MAS NMR spectrum of SMM (Fig. S8a) contains a single feature at -131 ppm, which can be assigned to F^- replacing OH^- groups in the structure close to sites with two Al atoms and a vacancy as nearest neighbors ($\text{Al-Al}-\square$; \square represents a vacant octahedral site) [60]. For Ni-SMM-1.8F, we would expect to see two resonances. Its spectrum is characterized by spinning sidebands which is common for ^{19}F due to its large chemical shift anisotropies. The band at -131 ppm is weaker than in SMM, which is reasonable because of the lower occurrence of $\text{Al-Al}-\square$ configurations in this Ni-containing clay. The spectrum does not contain any indication of other F^- species that coordinate to Ni^{2+} , which is expected given the magnetic nature of Ni. In such positions, the F will directly interact with the Ni, precluding its observation by ^{19}F NMR. Another factor could be the very low content of these $[\text{Ni}^{2+}\text{-F}]^+$ substitutions. After reduction of Ni-SMM-1.8F, a new band appears at -154 ppm. We cannot draw any firm conclusions from the spectra of the reduced Ni-SMM clay, but we surmise that reduction of structural Ni^{2+} at the surface and segregation into Ni^0 metallic clusters renders part of the structural F groups visible.

Our model can explain the following experimental findings. SMM clay contains only one type of BAS with an intrinsic strength close to that of zeolite protons. SMM is a dioctahedral clay with only Al^{3+} in the octahedral layer, which does not contain enhanced acid sites despite the F in the structure. In this case, F ions can only replace OH anions in the clay structure. This is in accord with the low F content of SMM. When Ni is introduced in the gel without fluoride, the acidity of the Ni-SMM material is very similar to that of SMM. In this clay, the octahedral layer of Ni-SMM consists almost exclusively of octahedral Ni cations. With increasing F content, mixed dioctahedral-trioctahedral Ni-SMM clays are formed that contain both octahedral Al and Ni cations. Note that, in principle, the replacement of $[\text{Al}^{3+}\text{-O}]^+$ by $[\text{Ni}^{2+}\text{-F}]^+$ allows forming a

dioctahedral clay. From the position of the (060) reflection of the Ni-SMM clays, we derive that the Ni-SMM clays are dioctahedral-trioctahedral mixtures.

We argue that the role of F anions during clay synthesis is twofold. Firstly, the rate of precipitation of Al- and Ni-hydroxides is limited so that, instead, more Ni-SMM clay can be formed. The larger amount of clay results in an increase of the number of BAS. Secondly, $[\text{Al}^{3+}\text{-O}]^+ \rightarrow [\text{Ni}^{2+}\text{-F}]^+$ substitutions can occur during Ni-SMM synthesis in the presence of fluoride, which generate a second type of interlayer BAS. The DFT calculations clearly show that F in bridging positions enhances the acidity of the interlayer BAS; this is in very good agreement with the experimental IR data. We expect that fluoride will also be present at positions where it replaces structural OH groups. The DFT calculations show that these substitutions do not lead to enhanced acidity.

We will briefly revisit some earlier interpretations on the acidity of Ni-SMM clay. Several authors indicated that high acidity is due to reduction of the Ni cations in the Ni-SMM structure. Heiner et al. established that reduction results in higher acidity and increased hydroisomerization activity [16]. These conclusions were drawn for a sample similar to our Ni-SMM-0.18F sample. We speculate that H_2 treatment led to the reduction of Ni^{2+} ions present at cation-exchange positions in the interlayer to Ni metal, thereby generating acidic protons. This explanation is in line with conclusions drawn for Ni-saponites by Geus and co-workers [17]. For our optimum Ni-SMM-1.8F sample, we have shown that the amount of strong BAS is similar for the calcined and the reduced sample. We also observed that a small fraction of Ni^{2+} in Ni-SMM-1.8F can be reduced at 440°C . Our XPS data support that these Ni^{2+} ions were present in the SMM structure. It is therefore reasonable to conclude that Ni^{2+} reduction will be limited to the edges of the clay platelets. This reduction results in some damage to the clay structure as suggested by XRD. Part of the resulting metallic Ni phase is present as very small clusters, which are highly reactive to traces of oxygen. In our view, there is no need to invoke BAS located at the edges of the clay platelets in explaining the enhanced acidity of Ni-SMM [24]. In support of this, we found by EPR spectroscopy that, unlike

Ni⁰ supported on an acidic silica-alumina, no Ni⁺ ions were formed. This strongly suggests that the BAS are not located at the clay edges where the Ni⁰ clusters are formed.

The acidity of the optimum fluoride-modified Ni-SMM sample is very similar to the enhanced acidity in H-USY zeolites. It is widely assumed that the enhanced acidity in H-USY zeolites relates to extraframework Al species present close to the BAS; the acidity is increased by withdrawing electron density from the bridging O atom to which the proton binds. We suspect that the F anions present in the clay structure directly attached to the tetrahedral Al atoms act in a similar manner. Although the inclusion of F in zeolites is well known, these fluoride species are usually removed during the calcination treatment. Different from zeolites, the F anions in Ni-SMM clay remain in the structure, because they bridge between octahedral Ni and tetrahedral atom or replace OH[−] groups.

4. Conclusion

Ni-SMM clays were synthesized with varying F content of the synthesis gel. The crystallinity of the clay samples increased with the F gel content. At low F content, aluminium and nickel hydroxides precipitation competes with slow clay formation. At too high F content, AlF₃ precipitates. At intermediate F gel content, a relatively phase-pure Ni-SMM clay is obtained that outperforms zeolites in *n*-heptane hydroisomerization. Characterization by IR spectroscopy with different probe molecules shows that these clays contain two types of BAS. In addition to acid sites that are similar to those observed in other clays and amorphous silica-alumina, Ni-SMM contains a very small population of BAS that display much stronger acidity, exceeding the acidity of zeolites. Notably, a small number of these strong acid sites renders Ni-SMM more active than zeolite. The density of these strong BAS does not depend on reduction of Ni-SMM. Under reducing conditions, a small amount of reduced Ni is formed, originating from Ni²⁺ at cationic exchange positions and octahedral Ni²⁺ at the edges of the clay platelets. Quantum-chemical calculations show that the substitution of octahedral [Al³⁺-O]⁺ → [Ni²⁺-F]⁺ causes high acidity of the interlayer proton connected to the aluminium-occupied tetrahedron. Consistent with the experimental data, a Ni-beidellite (no F in the structure) and beidellite with F (no Ni in the structure; F replaces structural OH) display conventional clay acidity. The role of Ni and F in obtaining highly acidic Ni-SMM is to enable the isomorphous substitution of bridging O anions that connect the octahedral with the tetrahedral layer by F. These findings show that there is room for the development of materials with higher acidity than aluminosilicates.

Acknowledgements

The authors thank Shell Global Solutions for financial support. The authors acknowledge technical assistance by Adelheid Elemans for elemental analysis, Tiny Verhoeven for XPS analysis and Anton Litke for XRD measurements.

Appendix A. Supplementary data

Supplementary data associated with this article can be found, in the online version, at <http://dx.doi.org/10.1016/j.apcatb.2016.03.006>.

References

- [1] A. Corma, *Chem. Rev.* 95 (1995) 559–614.
- [2] Q.L. Wang, G. Gianetto, M. Torrealba, G. Perot, C. Kappenstein, M. Guisnet, *J. Catal.* 130 (1991) 459–470.
- [3] J.T. Klopogge, S. Komarneni, J.E. Amonette, *Clays Clay Miner.* 47 (1999) 529–554.
- [4] M. Frenkel, *Clays Clay Miner.* 22 (1974) 435–441.
- [5] R.G. Capell, W.T. Granquist, US Patent 3252889 (1966), to Gulf Research Development Co.
- [6] A.C. Wright, W.T. Granquist, J.V. Kennedy, *J. Catal.* 25 (1972) 65–80.
- [7] J. Jaffe, US Patent 3803026 (1974), to Chevron Res.
- [8] J.R. Kittrell, G.E. Langlois, J.W. Scott, US Patent 3632501 (1972), to Chevron Res.
- [9] B.F. Mulaskey, U.S. Patent 3682811 (1972) to Chevron Res.
- [10] S.M. Csicsy, B.F. Mulaskey, US Patent 3655798 (1972), to Chevron Res.
- [11] K.H.W. Robschlager, C.A. Emeis, R.A. van Santen, *J. Catal.* 86 (1984) 1–8.
- [12] W.T. Granquist, U.S. Patent 3852405 1974 to NI Industries Inc.
- [13] W.T. Granquist, G.E. Hoffman, R.C. Boteler, *Clays Clay Miner.* 20 (1972) 323–329.
- [14] H.E. Swift, E.R. Black, *Ind. Eng. Chem. Prod. Res. Dev.* 13 (1974) 106–110.
- [15] T.R. Hughes, H.M. White, *J. Phys. Chem.* 71 (1967) 2192–2201.
- [16] J.L.L. Heinerman, L.L.C. Freriks, J. Gaaf, G.T. Pott, J.G.F. Collegem, *J. Catal.* 80 (1983) 145–153.
- [17] R.J.M.J. Vogels, J.T. Klopogge, J.W. Geus, *J. Catal.* 231 (2005) 443–452.
- [18] D.G. Poduval, J.A.R. van Veen, M.S. Rigutto, E.J.M. Hensen, *Chem. Commun.* 46 (2010) 3466–3468.
- [19] E.J.M. Hensen, D.G. Poduval, D.A.J.M. Ligthart, J.A.R. van Veen, M.S. Rigutto, *J. Phys. Chem. C* 114 (2010) 8363–8374.
- [20] R. Burch, *J. Catal.* 58 (1979) 220–229.
- [21] J.R. Sohn, A. Ozaki, *J. Catal.* 59 (1979) 303–310.
- [22] J.R. Sohn, A. Ozaki, *J. Catal.* 61 (1980) 29–38.
- [23] P. Falaras, F. Lezou, G. Seiragakis, D. Petrakis, *Clays Clay Miner.* 48 (2000) 549–556.
- [24] R.A. van Santen, *Rec. Trav. Chim.* 101 (1982) 157.
- [25] L.A. Bruce, J.V. Sanders, T.W. Turney, *Clays Clay Miner.* 34 (1986) 25–36.
- [26] F.M. Bautista, J.M. Campelo, A. Garcia, D. Luna, J.M. Marinas, A.A. Romero, J.A. Navio, M. Macias, *J. Catal.* 145 (1994) 107–125.
- [27] J.M. Campelo, A. Garcia, D. Luna, J.M. Marinas, *J. Catal.* 102 (1986) 299–308.
- [28] F.R. Chen, G. Coudurie, J.F. Joly, J.C. Vedrine, *J. Catal.* 143 (1993) 616–626.
- [29] R.B. Borade, A. Clearfield, *J. Chem. Soc. Faraday Trans.* 91 (1995) 539–547.
- [30] H. Hattori, O. Takashi, M. Takagi, K. Tanabe, *J. Catal.* 68 (1981) 132–143.
- [31] G. Kresse, J. Hafner, *J. Phys. Rev. B* 48 (1993) 13115–13118.
- [32] G. Kresse, J. Hafner, *J. Phys. Rev. B* 49 (1994) 14251–14269.
- [33] G. Kresse, J. Furthmüller, *Comput. Mater. Sci.* 6 (1996) 15–50.
- [34] G. Kresse, J. Furthmüller, *J. Phys. Rev. B* 54 (1996) 11169–11186.
- [35] J.P. Perdew, K. Burke, M. Ernzerhof, *Phys. Rev. Lett.* 77 (1996) 3865–3868.
- [36] P.E. Blöchl, *Phys. Rev. B* 50 (1994) 17953–17979.
- [37] G. Kresse, D. Joubert, *Phys. Rev. B* 59 (1999) 1758–1775.
- [38] H.J. Monkhorst, J.D. Pack, *Phys. Rev. B* 13 (1976) 5188–5192.
- [39] S. Grimme, J. Antony, S. Ehrlich, H. Krieg, *J. Chem. Phys.* 132 (2010) 154104–154119.
- [40] A. Viani, A.F. Gualtieri, G. Artioli, *Am. Mineral.* 87 (2002) 966–975.
- [41] J.A. Hriljac, M.M. Eddy, A.K. Cheetham, J.A. Donohue, G.J. Ray, *J. Solid State Chem.* 106 (1993) 66–72.
- [42] L. Huve, R. Le Dred, D. Saehr, J. Baron, *Synthesis of Porous Materials: Zeolites, Clays, and Nanostructures*, Dekker, New York, 1997, p. 465.
- [43] L. Huve, R. Le Dred, D. Saehr, J. Baron, *Synthesis of Microporous Materials*, Van Nostrand, New York, 1992, p. 202.
- [44] C. Alonso, A. Morato, F. Medina, F. Guirado, Y. Cesteros, P. Salagre, J.E. Sueiras, *Chem. Mater.* 12 (2000) 1148–1155.
- [45] H.E. Swift, in: J.J. Burton, R.L. Garten (Eds.), *Advanced Materials in Catalysis*, Academic Press, New York, 1977, pp. 213.
- [46] L. Qu, W. Zhang, P.J. Kooyman, R. Prins, *J. Catal.* 215 (2003) 7–13.
- [47] H. Wang, X. Kou, J. Zhang, J. Li, *Bull. Mater. Sci.* 31 (2008) 97–100.
- [48] P.A. Jacobs, H. Nijs, J. Verdonck, E.D. Derouane, J.-P. Gilson, A.J. Simoons, *J. Chem. Soc. Faraday Trans.* 75 (1979) 1196–1206.
- [49] A. Brückner, U. Bentrup, H. Zanthoff, D. Maschmeyer, *J. Catal.* 266 (2009) 120–128.
- [50] E.J.M. Hensen, D.G. Poduval, D.A.J.M. Ligthart, J.A.R. van Veen, M.S. Rigutto, *J. Catal.* 269 (2010) 201–218.
- [51] X. Zhu, L. Wu, P.C.M.M. Magusin, B. Mezari, E.J.M. Hensen, *J. Catal.* 327 (2015) 10–21.
- [52] J. Datka, A.M. Tutek, J.H. Jehng, I.E. Wachs, *J. Catal.* 135 (1992) 186–199.
- [53] K. Mohana Rao, G. Spoto, A. Zecchina, *Langmuir* 5 (1989) 319–325.
- [54] N. Echoufi, P. Gelin, *J. Chem. Soc. Faraday Trans.* 88 (1992) 1067–1073.
- [55] M. Maache, A. Janin, J.C. Lavalley, J.F. Joly, E. Benazzi, *Zeolites* 13 (1993) 419–426.
- [56] O. Cairon, T. Chevreau, J.C. Lavalley, *J. Chem. Soc. Faraday Trans.* 94 (1998) 3039–3047.
- [57] L.W. Beck, T. Xu, J.B. Nicholas, J.F. Haw, *J. Am. Chem. Soc.* 117 (1995) 11594–11595.
- [58] K. Chakarova, K. Hadjiivanov, *Chem. Commun.* 47 (2011) 1878–1880.
- [59] A. Takagaki, M. Sugisawa, D. Lu, J.N. Kondo, M. Hara, K. Domen, S. Hayashi, *J. Am. Chem. Soc.* 125 (2003) 5479–5485.
- [60] A. Labouriau, Y.W. Kim, S. Chipera, D.L. Bish, W.L. Earl, *Clays Clay Minerals* 43 (1995) 697–704.